5-2012

Subsurface characterization using ground-penetrating radar in a hydrologically active vadose zone

Adam Mangel
Clemson University, amangel@clemson.edu

SUBSURFACE CHARACTERIZATION USING GROUND-PENETRATING RADAR IN A HYDROLOGICALLY ACTIVE VADOSE ZONE

A Thesis
Presented to
the Graduate School of
Clemson University

In Partial Fulfillment
of the Requirements for the Degree of
Master of Science
Hydrogeology

---

by
Adam Robert Mangel
May 2012

Accepted by:
Dr. Stephen M.J. Moysey, Committee Chair
Dr. Lawrence C. Murdoch
Dr. Ronald W. Falta

Abstract

Three experiments were conducted to measure the ability of ground-penetrating radar (GPR) to non-invasively determine water content while simultaneously resolving depth to wetting fronts, buried objects, and stratigraphic boundaries during dynamic hydrologic conditions. This is particularly appealing as GPR can provide dense spatial coverage for vadose zone characterization where traditional invasive measurements are costly, destructive, and time-consuming. The vadose zone was replicated using a tank filled with 1) homogeneous river sand, 2) homogeneous river sand with an embedded land mine surrogate, and 3) homogeneous river sand with an embedded layer of silica flour. These systems were subjected to controlled irrigation events and monitored with GPR using automated time-lapse wide-angle reflection refraction (WARR) surveying. The unique form of data collection allowed the data to be conceptualized into a 3D data cube, providing multi-offset projections to extract wave velocities for depth and average water content measurements and transient common-offset projections to observe changes in amplitude and traveltime of arrivals over time associated with the fluctuations in average water content of the tank.

Average water content estimates from ground-penetrating radar were similar to in-situ capacitance probe measurements for the homogeneous tank experiment. Radar estimates of depth to wetting front and bottom of the tank, however, were found to have some issues associated with wave interference, causing errors in the range of 1-25%, with

the largest errors occurring at times of infiltration. It was concluded that GPR has potential, through transient multi-offset imaging of the subsurface, to greatly improve vadose zone characterization by imaging the subsurface, quantifying water content, and tracking wetting fronts as they move through the media.

The layered experiment revealed that the silica flour greatly inhibits vertical flow of water causing significant changes in the GPR response through time when compared to a similar homogeneous experiment. At initial conditions, the radar data resembled that of a single layer system; however, as the water content increased, reflections and multiples from the upper layer dominated the image, degrading the interpretation of the system and clearly illustrating that interpretation of GPR data can be affected by the hydrologic state of the subsurface.

The land mine experiment showed that the unsaturated flow of water was not affected by the land mine and closely resembled the hydrologic response of the homogeneous tank. While the land mine signal was unclear on the GPR data, differences in amplitude vs. offset relationships between groundwave arrivals for the land mine and homogeneous tank indicate that significant changes in amplitude occur which may assist present methods for landmine identification. The data also showed that high water content values, such as after a rainfall event, provide a more favorable environment for landmine identification, as the groundwave is highly attenuated, reducing wave interference. While valuable data was collected, WARR surveying of the land mine may be secondary to common offset or common mid-point surveying as the land mine was not

clearly visible on the WARR data, however, more robust signal processing of WARR data may also improve data interpretation. In conclusion, these experiments have illustrated that more reliable images, water content estimates, and overall characterization of the subsurface will be attained by the transient monitoring of the subsurface with surface based GPR for variable hydrologic conditions.

Dedication

This thesis is dedicated mainly to my Mother, Robin L. Mangel, and Father, Thomas L. Mangel, for allowing me every opportunity possible. Without your encouragement, hard work, perseverance and overall knowledge of life that you imparted on me, I would not be half of what I am today, and for that I sincerely thank you. I would also like to mention thanks to my Brother, Nicholas, and my two Sisters, Kristy and Katie for all their love and support through the years. Lastly, I would like to that all of my colleagues, past, present, and future, for their continued support.

Acknowledgements

This material is based upon work supported by, or in part by, the U.S. Army Research Laboratory and the U.S. Army Research Office under grant number W911NF-08-1-0370 and W911NF-10-1-0292.

TABLE OF CONTENTS

Page

List of Tables and Figures

1. Applying surface-based ground-penetrating radar surveys to characterization of the vadose zone

Abstract

This research focuses on the use of ground-penetrating radar (GPR) to determine the hydrologic state of the vadose zone. This was done using time-lapse measurements during hydrologic perturbations, which allowed quantification of volumetric water content and coincident imaging of wetting fronts and physical (stratigraphic) boundaries. Volumetric water content (VWC) and heterogeneity are important properties of the vadose zone that have a large effect on the fate and transport of infiltrating water and hazardous chemicals. Electromagnetic waves are highly sensitive to water content, which allows us to non-invasively measure VWC with GPR, attaining accuracy comparable to more common, costly, invasive, and spatially limited methods. Dynamic processes, e.g. infiltration, when imaged with time-lapse radar measurements, shed light on preferential flow paths, giving insight into the stability of wetting fronts and the resulting distribution of water, which can be used to calibrate hydrologic models, assisting in the fate and transport of hazardous chemical spills. Although there are errors associated with VWC estimates from surface based GPR, and questions about the signatures of wetting fronts on GPR data, current studies show promise for alleviating these errors and establishing GPR as a commonly used tool for effectively and efficiently characterizing the vadose zone over large areas. To identify these issues and provide a

further understanding, three experiments including 1) homogenous, 2) layered heterogeneous, and 3) object heterogeneous systems are imaged using a two-dimensional surface based multi-offset radar survey during steady-state, infiltration, and recovery conditions.

1.1. Introduction

The movement of fluids through the vadose zone is highly dependent on the volumetric water content, θ, of the media (Richards 1931) and the connectivity of pore spaces (Looney and Falta, 2000). Detailed characterization is limited by common sampling methods which are costly, destructive, invasive, and spatially limited; e.g. direct sampling followed by lab analysis (Ellsworth et al., 1991, Mallants et al. 1996), tracer tests (Wirenga et al., 1991, Scanlon, 1992), infiltrometer tests (Angullo-Jaramillo et al., 2000, Mohanty et al., 1994, Simunek and VanGenuchten, 1996), any of which may contain some form of computational effort for predicting parameters between sample points. This leaves characterization of the vadose zone susceptible to spatial averaging and assumptions of homogeneity, which may mislead conclusions for a given site.

Vadose zone dynamics are paramount to hydrologic based fields of study such as agriculture (McLay et al., 2001, Secunda et al., 1998), and contaminant fate and transport (Brewster et al., 1995, Glass and Nicholl, 1996, Oostrom et al., 2003, Pantazidou and Sitar, 1993). McLay et al. (2001) even go so far as to state that the permeability of the vadose zone is the most important parameter in their study of determining agricultural based nitrate contamination. Glass and Nicholl (1996) point out that the fingering of fluids moving through unsaturated media is nearly impossible to avoid, especially with

three-phase systems (liquid/gas/non-aqueous phase liquid (NAPL)), which are common at vadose zone NAPL spill sites. Where geostatistics can offer a measure of uncertainty (Goovaerts, 1999), GPR offers robust and reliable data to reduce uncertainties and errors from spatial averaging.

I propose that ground-penetrating radar (GPR), which has been established as an effective tool for determining volumetric water content (Greaves et al., 1996, Huisman et al., 2001, Husiman et al., 2003, van Overmeeren et al., 1997) due to sensitivity of electromagnetic (EM) wave velocity to VWC (Topp et al., 1980), is solution viable method for the non-invasive, robust characterization of the vadose zone. Previously and extensively used for stratigraphic studies (Davis and Annan, 1989, van Overmeeren, 1998, Van Dam and Schlager, 2000), advances in GPR technology have broadened applications to environmental and hydrologic applications (Knight, 2001, Neal, 2004). Hubbard et al. (1997), along with Beres and Haeni (1991) and Gloaguen et al. (2001), conclude that sparse conventional hydrologic data coupled with dense 2-D or 3-D geophysical data has potential of significantly improving hydraulic parameter estimates over the hydrologic data alone.

Surface-based GPR data is collected using a transmitter and receiving antenna at a fixed distance apart. Subsurface discontinuities in electrical properties are responsible for the reflection of electromagnetic (EM) waves, which allows them to be recorded in time by the receiving antenna. These reflections coincide with stratigraphic boundaries in static environments (Neal, 2004), but may also be the response of a propagating wetting front as seen by Vellidis et al. (1990). Since this data was collected at one antenna offset

and one location, they could not determine water content variability over the site, but instead used a buried pipe to estimate wave velocity and register their images with depth. To alleviate this limitation, multi-offset data is employed.

Multi-offset GPR data is typically interpreted with normal move-out analysis (NMO), using data collected at multiple antenna offsets to determine the electromagnetic (EM) wave velocity, which is then used to convert the time domain to depth, creating an image of the subsurface. The wave velocity can also be used to determine water content using the Topp Equation (Topp et al., 1980) or a calibrated petrophysical relationship; however, uncertainties remain around the effect of variable VWC on surface-based GPR data. Seasonal variability of VWC in the vadose zone has been the focus of some studies (Lunt et al., 2005, Steelman and Endres, 2010), while others focus on more transient events such as infiltration (Grote et al., 2005, Haarder et al., 2011, Moysey, 2010, Saintenoy et al., 2007) or precision agriculture (Freeland et al., 1998). Steelman and Endres (2010) studied the variability in VWC using the groundwave from multiple radar frequencies over a year and compared them to gravimetric VWC measurements. Lunt et al. (2005) used reflected arrivals on common offset data with supplemental borehole information to track seasonal changes in VWC at a vineyard. Haarder et al. (2011) used a dyed tracer along with time-lapse surface based GPR to measure changes in response for days after a two hour infiltration event. Specifically, Lunt et al (2005) attributed errors in VWC estimates (0.018 % RMSE) to wave interference and errors in the depth estimates of the reflector, which were accurate to 0.05m, while van Overmeeren et al. (1997) attributed errors in VWC estimates (0-3%) to empirical VWC/EM wave velocity

relationships rather than calibrated equations which were used in Lunt et al. (2005). Huisman et al (2001) stated that errors in VWC (0.0281% RMSE) were caused by uncertainty in EM wave velocity. Booth et al., 2010, state that an error in semblance analysis itself, which can be accounted for, is the cause of underestimated velocities. Although Haarder et al. (2001) never directly determined VWC from radar data, due to a limitation by the geometry of the radar data collection, significant reflection data was collected from an extremely heterogeneous wetting front and subsequent heterogeneous VWC pattern. Attempting to understand errors in water content estimates and recognize signatures of stable or instable wetting fronts to delineate preferential flow paths and subsurface heterogeneities on surface based GPR data, is the basis for this research.

For this research, I will be following the approach of Moysey (2010), who concluded that arrivals on common offset radar data have specific trajectories associated with changes in VWC through monitoring of a 150 minute infiltration event with common offset GPR at 3 second intervals. In supplement to Moysey (2010), I have conducted multiple experiments in a sand tank using automated multi-offset GPR data collection, to determine EM wave velocities, coupled with controlled flux irrigation. Three experiments will be outlined in this thesis showing the GPR response of our analogous vadose zone during infiltration events for 1) a homogenous system, 2) a thin layer heterogeneous system, and 3) a buried land mine simulant. It is our hypothesis, that these experiments will further the understanding of the effect of variable VWC on surface based GPR data, shed light on errors associated with data interpretation and analysis, and

provide a solid foundation for further study concerning heterogeneous systems and the instability of unsaturated flow.

1.2. Unsaturated Flow and Infiltration Theory

The vadose zone is defined as the upper most volume of the subsurface, including all material above the groundwater table that is below saturation and subject to capillary forces. Fluid flow in the unsaturated zone is governed by Richards Equation (Richards, 1931). This equation is used throughout this thesis to model the hydrologic response of the vadose zone to perturbations from irrigation using HYDRUS-1D and SWMS-3D models. For 1D unsaturated vertical flow

$$\frac{\partial \theta}{\partial t} = \frac{\partial}{\partial z}\left[K(h)\left(\frac{\partial h}{\partial z} + 1\right)\right] \tag{1.1}$$

where θ is the volumetric water content, h is the soil-water pressure head, K is the unsaturated hydraulic conductivity, z is the vertical distance, and t is time. For three dimensions

$$\frac{\partial \theta}{\partial t} = \frac{\partial}{\partial x_i}\left[K\left(K_{ij}^{A}\frac{\partial h}{\partial x_j} + K_{iz}^{A}\right)\right] - S \tag{1.2}$$

where S is a sink term, and x, y, and z are spatial coordinates (Simunek et al., 1995).

Unsaturated hydraulic conductivity (K) can also be expressed as a function of θ

$$K(\theta) = \theta^{2}\left[1 - \left(1 - \theta^{1/m}\right)^{m}\right] \tag{1.3}$$

where m is $1\text{-}2/n$ and n is a shape parameter determined from fitting data points to a water retention curve model (van Genuchten, 1980).

For this study, the relationship that hydraulic conductivity has with volumetric water content, along with other parameters, is determined through water retention curve experiments and the van Genuchten equation (van Genuchten, 1980).

$$\theta = \theta_r + \frac{(\theta_s - \theta_r)}{[(1+\alpha h)^n]^m} \tag{1.4}$$

where θ_r is the residual volumetric water content, θ_s is the saturated volumetric water content (porosity), α is the air entry parameter, and *n* and *m* are shape parameters with the relationship *m = 1-1/n*. This model is fitted to the experimental data through a sum of squared error minimization to give us predicted values for the aforementioned parameters.

1.3. Maxwell's Equations

Surface-based ground-penetrating radar is used to noninvasively determine the transient electrical response of the subsurface to an incident pulse of electromagnetic energy. The fundamentals of how the electromagnetic field changes in response to the electromagnetic properties of the subsurface are based in electromagnetic theory. The equations which govern this behavior are known as Maxwell's equations (Maxwell, 1861, 1862). The equations are:

$$\overline{\nabla} \mathrm{X} \overline{E} = -\frac{\delta \overline{B}}{\delta t} \tag{1.5}$$

$$\overline{\nabla} \mathrm{X} \overline{\mathrm{H}} = \overline{\mathrm{J}} + \frac{\delta \overline{D}}{\delta t} \tag{1.6}$$

$$\overline{\nabla} \ \mathrm{X} \ \overline{\mathrm{D}} = q \tag{1.7}$$

$$\overline{\nabla} \cdot \overline{\mathrm{B}} = 0 \tag{1.8}$$

where $\overline{E}$ is the electric field strength vector, q is the electric charge density, $\overline{B}$ is the magnetic flux density vector, $\overline{J}$ is the electric current density vector, $\overline{D}$ is the electric displacement vector, t is time $\bar{B}$ is the magnetic flux density vector, and $\overline{H}$ is magnetic field intensity. Equations 1.4-1.7 are essentially a compilation of Gauss's, Ampere's, Faraday's and the Lorentz force laws. The electric current density, electric current displacement, and magnetic flux density vectors are known as the constitutive equations and solved according to:

$$\bar{J} = \tilde{\sigma}\bar{E} \tag{1.9}$$

$$\bar{D} = \tilde{\varepsilon}\bar{E} \tag{1.10}$$

$$\bar{B} = \tilde{\mu}\bar{E} \tag{1.11}$$

where σ is electrical conductivity, ε is dielectric permittivity, and μ is magnetic permeability. These three physical properties govern how EM waves propagate through any material. Maxwell's equations are used extensively in this thesis to model GPR response to a variety of hydrologic conditions using a 2D finite-difference time domain code developed in MATLAB (Irving and Knight, 2006).

Since the use of GPR is most common in low-loss materials, where σ and μ are low and allow the transmission of EM waves, σ and μ are of lesser concern to practitioners. In relatively conductive settings, where σ and μ cause the EM waves to attenuate into current, GPR surveys are lacking in returned signal and therefore must be analyzed with other methods. Electrical conductivity (σ) is usually only taken into consideration in clay-rich or saline environments (high electrical loss) where wave attenuation may be a problem, while magnetic permeability (μ) may be accounted for in

the presence of magnetic ore bodies. This leaves dielectric permittivity as the main property governing wave propagation, which is often normalized by the dielectric permittivity of air ($8.89E-12\ Fm^{-1}$) to give the dielectric constant κ. A petrophysical equation relating this parameter to water content can be derived through calibration experiments since this parameter has a high correlation with water content (Topp et al., 1980). This parameter is related to the velocity (v) of the EM wave using

$$v = \frac{c}{\sqrt{\kappa}} \tag{1.12}$$

where c is the speed of light in a vaccum ($0.3mns^{-1}$). This relationship, coupled with the Topp Equation (Topp et al., 1980) forms the fundamental relationship that allows the estimation of water content with GPR.

Solving Maxwell's equations will yield the intensity of the electromagnetic wavefield. The wavefield can consist of wavefronts which are incident, reflective, and/or refractive. Wavelength, which is related to the resolution of radar surveying, can be calculated by

$$\lambda = \frac{v}{f} \tag{1.13}$$

Depending on what a GPR survey is attempting to image, the frequency of the incident radar signal can be changed to offer higher or lower resolution, maintaining that the resolution is on the order of λ/4 (Jol, 2009).

The point of origin of the EM energy and how the response is measured and subsequently interpreted are highly dependent on survey geometry. For this research, we will focus on the wide-angle reflection refraction (WARR) survey, but will also make

references to common-offset profiling and common mid-point (CMP) surveys, which will now be discussed in detail. For details of EM wave theory for GPR, refer to Jol (2009).

1.4. Ray Paths: Direct, Reflected, and Refracted

In order to understand more clearly what radar data are depicting, significant arrivals on radar data are conceptualized as ray paths. It is paramount to this research and all GPR data analysis that a comprehensive understanding of these arrivals is achieved. A ray path is always perpendicular to wavefronts, and always originates at a transmitter and terminates at a receiver. Figure 1.1 shows ray paths for a single offset x, a reflector depth z, and an EM wave velocity v_{rms}, and their associated arrivals on common offset and multi-offset projections (CMPs and WARRs). Two direct arrivals; the airwave (A) and the groundwave (B) are represented by rays that move through the air and ground directly to the receiver, respectively. The reflected arrival (C) travels to an interface and back to the receiver, while the air-refracted reflection arrival (D) travels to the interface and back into the air before arriving at the receiver. The refracted arrival (E) travels into a lower layer, back through the first layer then to the receiver. While ray paths can be infinite, these are the most common and the basis for understanding and interpreting GPR data.

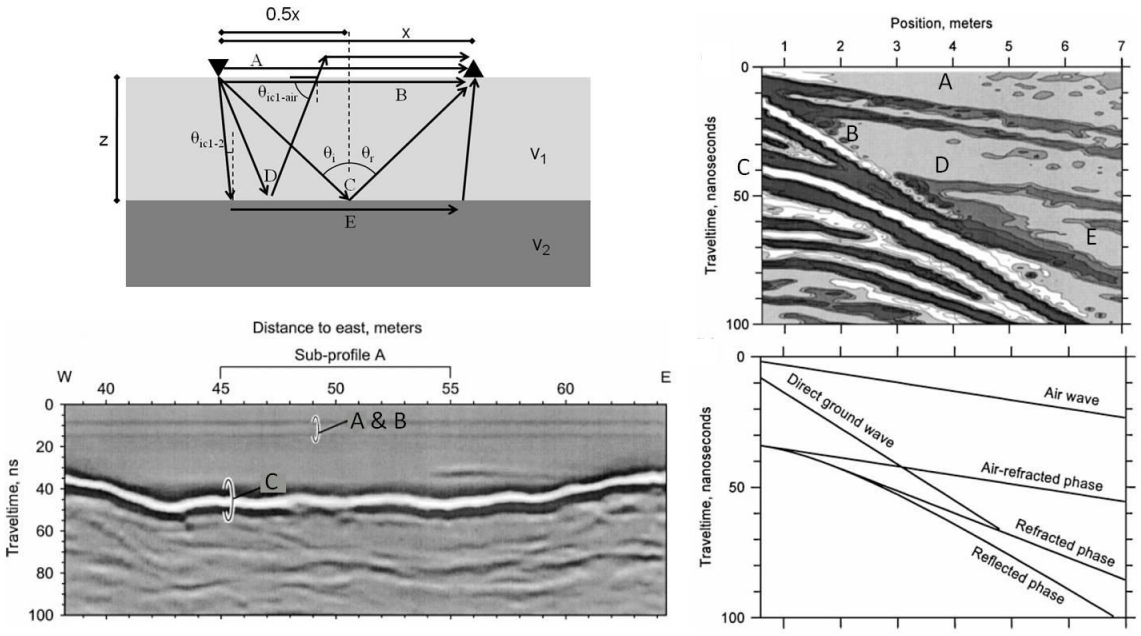

Figure 1.1: Raypath conceptualization of EM waves showing specific arrivals on radar data (A = airwave, B = groundwave, C = reflection, D = air-refracted reflection, E = layer refraction) from Bohidar and Hermance (2002). Transmitter is represented by an inverted triangle and receiver is represented by an upright triangle.

1.4.1. The Airwave

The airwave (A) (Figure 1.1) is commonly ignored in GPR data, however, it can be used to calibrate or correct traveltime errors, referred to as the time-zero correction, from triggering delays on the GPR data. Since we know the EM wave velocity of air, v_{air}= 0.3mns^{-1}(speed of light in vaccum), we can calculate the traveltime (*tt*) of the airwave accordingly

$$tt = \frac{x}{v_{air}} \tag{1.14}$$

thereby producing calculated and measured traveltime at each offset, correcting discrepancies in the data due to a delay in the system.

1.4.2. The Groundwave

The groundwave (B) (Figure 1.1) samples the uppermost part of the subsurface referred to as the Fresnel zone (Jol, 2009).

$$Fresnel\ Zone = \frac{\sqrt{\lambda x}}{2} \tag{1.15}$$

At small offsets, the groundwave is difficult to delineate due to interference with the airwave. Being direct arrivals, the airwave and groundwave have linear trends on multi-offset data. Travel time of the groundwave is calculated by substituting v_{ground} for v_{air}. Although this arrival has been the subject of some analysis (Grote et al., 2010, Huisman et al. 2003) and some skepticism (van der Kruk, 2006), it remains a valuable piece of data.

1.4.3. The Reflected Wave

Reflections (C) (Figure 1.1) are the main focus for this thesis and for most practitioners as they hold data about depth to a reflector and root mean squared EM wave velocity (v_{rms}) of the layer(s). Tracing the ray from the transmitter to the point at which the reflection takes place is derived using Fermat's principle (Pierre de Fermat 1601-1665), or the principle of least time (Burger et al., 2006).

For a reflected ray path, for a single layer model, the traveltime equation is

$$tt = \frac{\sqrt{(x^2+z^2)}}{v_1} + \frac{\sqrt{y^2+z^2}}{v_1} \tag{1.16}$$

For the shortest time we take the first derivative and set it equal to zero

$$\frac{dt}{dx} = \frac{x}{v_1\sqrt{(x^2+z^2)}} - \frac{y}{v_1\sqrt{(y^2+z^2)}} = 0 \tag{1.17}$$

Using the basic trigonometry identities

$$\sin\theta_1 = \frac{x}{\sqrt{(x^2+z^2)}} \quad \text{and} \quad \sin\theta_2 = \frac{y}{\sqrt{(y^2+z^2)}} \tag{1.18}$$

Plugging these in

$$\frac{\sin\theta_1}{v_1} - \frac{\sin\theta_2}{v_1} = 0 \tag{1.19}$$

Therefore, $\theta_1$must equal θ_2 and *x* must equal *y* meaning that the reflection point is halfway between the transmitter and receiver. Now that we know this, Eq. 1.16 can be simplified to

$$tt = \frac{2\left[\left(\frac{x}{2}\right)^2 + z^2\right]^{0.5}}{v_{rms}} \tag{1.20}$$

Equation 1.20 is known as the normal move-out equation (Yilmaz, 1987, Jol, 2009), which has the distinguishing characteristic of a hyperbolic trajectory, which helps us both recognize the arrivals and analyze the GPR data.

1.4.3.1. Normal Move-out Analysis

Normal move-out (NMO) analysis is an essential part of multi-channel GPR data analysis. NMO analysis uses a linearized version of Eq. (1.20) to determine the EM wave velocity from reflections on multi-offset GPR data. If we square both sides of Eq. (1.20)

$$tt^2 = \left(\frac{1}{v_{rms}^2}\right)x^2 + \frac{4z^2}{v_{rms}^2} \tag{1.21}$$

We now have a linear equation with $\frac{1}{v_{rms}^2}$ as the slope and $\frac{4z^2}{v_{rms}^2}$ as the intercept, allowing us to use the linear least-squares regression method to minimize the error between data points and solve for v_{rms} and z giving us a best estimate for the parameters. Data points are determined using patterns of arrivals on GPR data and reflect the two-way traveltime of the EM energy that originated at the transmitting antenna.

GPR data analysis has its roots in seismic data analysis as many of the tools practitioners use were developed by seismologists for energy exploration. Available techniques for seismic analysis can be found in Yilmaz (1987) and their GPR equivalents in Jol (2009).

1.4.4. Refracted Waves

Rays returning to the surface, other than the reflection ray, are refracted by the increase in EM wave velocity from the ground to the air and form the air-refracted reflection arrival (D) (Figure 1.1). This relationship is described by Snell's Law

$$\frac{\sin\theta_i}{\sin\theta_r} = \frac{v_i}{v_r} \tag{1.22}$$

where θ_i is the incident angle (measured from normal), v_i is the upper layer velocity, θ_r is the refracted angle (measured from normal), and v_r is the lower layer velocity. In order for the ray path to return to the receiver, the angle of refraction must equal 90˚, and since the sine of 90˚ is one, Eq. 1.21 simplifies to

$$\theta_{ic} = \sin^{-1}\left(\frac{v_i}{v_r}\right) \tag{1.23}$$

where θ_{ic} is the critical angle of incidence which causes a 90˚ refraction. These arrivals are typically hard to see on common offset data due to the minimal separation of the antennas, not allowing the recording of the refracted energy.

Refracted arrivals (E) (Figure 1.1) are commonly not seen due to the fact that EM wave velocity typically decreases with depth, negating any chance of seeing this arrival. However, in special cases such as this research, where we are tracking the movement of a wetting front through the vadose zone, the EM wave velocity behind the wetting front is typically lower than the EM wave velocity ahead of the wetting front, thus providing an opportunity to generate such an arrival. It is, however, subject to the same caveats as the aforementioned air-refracted reflection.

1.5. Radar Geometry

Time-domain surface based ground-penetrating radar (GPR) measures the transient electrical response of the subsurface to an incident pulse of electromagnetic energy at a specific frequency (1MHz – 1GHz). For a given antenna geometry, specific orientations of subsurface interfaces and objects have distinct patterns on the GPR data. For a complete reference to GPR data collection methods, refer to Jol (2009).

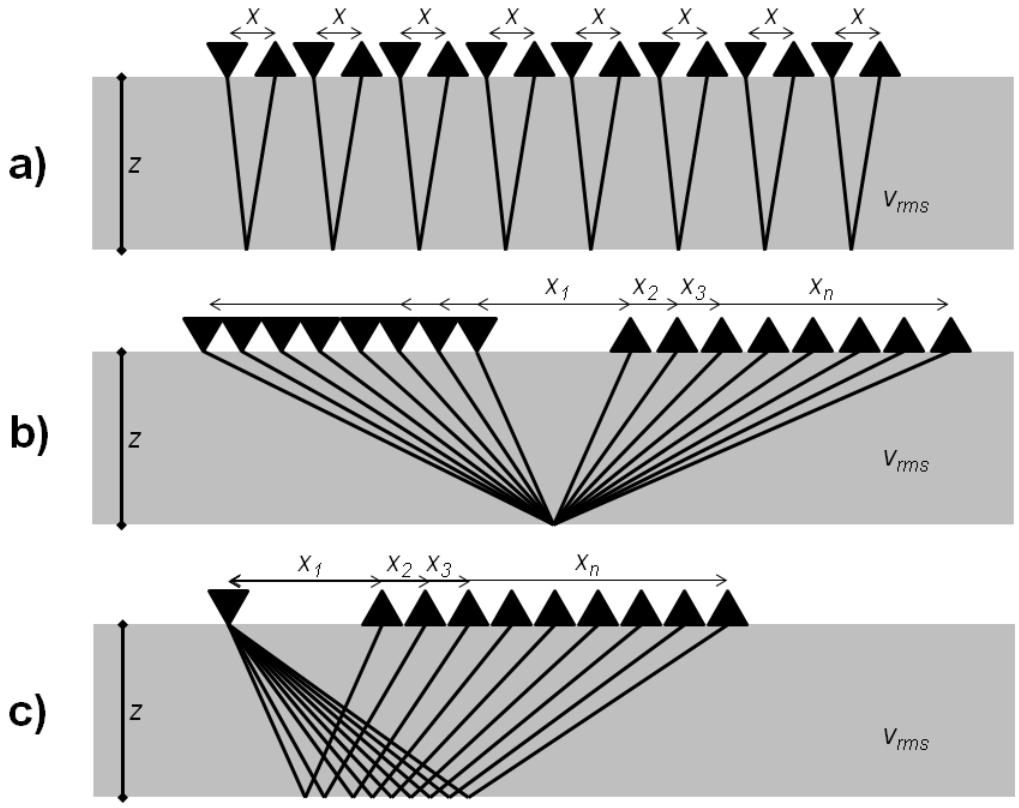

Figure 1.2: Antenna geometries for a) common offset, b) CMP, and c) WARR surveys showing antenna offset (x), average EM wave velocity (v_{rms}), and reflector depth (z). Transmitter is represented by an inverted triangle and receiver is represented by an upright triangle.. Transmitter is represented by an inverted triangle and receiver is represented by an upright triangle.

1.5.1. Common-Offset Profiling

Profiling surveys are employed over large areas due to the ease of data acquisition. To collect this data, antennas mounted to a sled, a fixed distance apart, are dragged over the surface (Figure 1.2a). Triggering is controlled manually, using an

odometer wheel, or at discrete time intervals. The limitation with this data, however, is that variations in the travel time of arrivals could be due to stratigraphic changes, or variations in EM wave velocity. Commonly, CMPs are employed at selected sites where common-offset data was collected to change the data from the time domain. This however, leaves the data susceptible to averaging and therefore, misinterpretation.

1.5.2. Common Mid-point Surveys (CMP)

Common mid-point surveys are typically employed when GPR data is being used to determine more robust data sets from the subsurface. These surveys are carried out by moving the antennas away from a central point at discrete step sizes to successively larger separations (Figure 1.2b). This survey allows us to perform a NMO analysis to determine EM wave velocity, which will be discussed in detail later.

1.5.3. Wide-Angle Reflection Refraction (WARR)

WARR surveys are very similar to CMPs in the sense that they are used to acquire more detailed information about the subsurface. This survey, however, consists of a stationary antenna, thus increasing the opportunity to reach the critical angle of incidence (Eqs. 1.22, 1.23), and generate a refracted arrival (Figure 1.2c). This geometry assumes constant EM wave velocity for the NMO analysis since this survey samples multiple points in the subsurface.

1.6. Summary

Ground-penetrating radar has been well established as a valuable tool for studying the electrical response of the upper 10m of the earth in low electrical loss environments.

Developments in system technology have advanced GPR into the hydrological and environmental realms as scientists have discovered that the electrical response, as measured by GPR, of the subsurface is especially sensitive to volumetric water content. This sensitivity allows practitioners to study the vadose zone in regards to VWC at different lengths of time, resulting in steady-state and time-lapse measurements on the scale of a few hours to an entire year. Short-term time-lapse measurements during hydrologic perturbations show promise for determining hydraulic flow parameters while steady-state and long-term measurements help with watershed balances and overall vadose zone characterization. Difficulties still remain, however, in quantifying the effect of variability of VWC on GPR data as differences between VWC estimates and more robust analytical methods, e.g. gravimetric analysis, exist, however, it has been established that through petrophysical relationships , like the Topp Equation, GPR can accurately image VWC and subsurface heterogeneities over large areas at a fraction of the cost of conventional, destructive, invasive, and spatially limited methods, thus providing a solution to errors caused by spatial averaging or disruption of the natural state of the subsurface. In conclusion, we hold that full three-dimensional imaging, and conceptualized two-dimensional imaging, regardless of the presence of supplementary data, is a strong method for determining VWC and observing dynamic processes such as infiltration and preferential flow.

2. Multi-offset ground-penetrating radar imaging of a lab-scale infiltration test

*A version of this paper has been published in Hydrology and Earth Systems Sciences Discussion Journal under the following citation and is under review for publication in Hydrology and Earth Systems Sciences:

Mangel, A.R., Moysey, S.M.J, Ryan, J.C., Tarbutton, J.A., "Multi-offset ground-penetrating radar imaging of a lab-scale infiltration test", Hydrology and Earth Systems Science Discussions, vol. 8, pp. 10095-10123, 2011.

Abstract

A lab scale infiltration experiment was conducted to evaluate the use of time-lapse multi-offset ground-penetrating radar (GPR) data for characterizing dynamic hydrologic events in the vadose zone. A unique GPR data acquisition setup allowed sets of 21 traces at different offsets to be recorded every 30 seconds during a 3 hour infiltration experiment. The result is a rich GPR data cube that can be viewed as multi-offset gathers at discrete moments in time or as common offset images that track changes in the GPR arrivals over the course of the experiment. These data allows us to continuously resolve the depth to soil boundaries while simultaneously tracking changes in wave velocity, which are strongly associated with soil water content variations. During the experiment the average volumetric water content estimated in the tank ranged between 0. 10-0.30 vol. vol.$^{-1}$ with discrepancies between the GPR results, moisture

probe data, and 1D numerical modeling on the order of 0.03-0.05 vol. vol.$^{-1}$, though the patterns of the estimated water content over time were consistent for both wetting and drying cycles. Relative errors in the estimated depth to a soil boundary located 60cm from the surface of the tank were typically on the order of 2% over the course of the experiment. During the period when a wetting front migrated downward through the tank, however, errors in the estimated depth of this boundary were as high as 25%, primarily as a result of wave interference between arrivals associated with the wetting front and soil boundary. Given that our analysis assumed one-dimensional, vertical infiltration, this high error could also suggest that more exhaustive GPR data and comprehensive analysis methods are needed to accurately image non-uniform flow produced during periods of intense infiltration. Regardless, we were able to track the movement of the wetting front through the tank and found a reasonably good correlation with in-situ water content measurements. We conclude that transient multi-offset GPR data are capable of quantitatively monitoring dynamic soil hydrologic processes

1. Introduction

Ground penetrating radar (GPR) has been established as a valuable tool for evaluating soil water content (Huisman et al., 2003). Surface-based radar reflection surveys are particularly appealing for this purpose as they can map large-scale regions that are relevant to field applications ranging from precision agriculture (Freeland et al., 1998, Lunt et al., 2005) to contaminant transport (Brewster et al., 1995). Several authors, including Lunt et al. (2005) and Grote et al. (2005), have shown that GPR reflection surveys can provide water content estimates with an accuracy comparable to traditional

invasive, spatially limited methods, e.g., time-domain reflectometry (TDR) or neutron probes. A significant advantage of these probes over radar, however, is that they can provide reliable water content estimates with high-temporal resolution, e.g., at time scales capturing the dynamics of individual infiltration events. In contrast, almost all studies using GPR to quantitatively estimate water content have been performed under nearly steady-state hydraulic conditions or where changes in water content have been observed over long periods of time, e.g., seasonally, due to the significant effort and time required for data collection (Lunt et al., 2005, Grote et al., 2005, Steelman and Endres, 2010)

Most common methods for estimating water content from GPR are based on deriving wave velocity from arrivals identified in radar images (Huisman et al., 2003). For example, Lunt et al. (2005) mapped seasonal changes in water content over an 80m x 180m area of a vineyard by evaluating variations in wave velocity determined from the traveltime of reflections produced by a clay layer of known depth, where the depth of the clay layer was inferred from borehole data. Water contents were then estimated from the velocities using a site-specific petrophysical equation. Following a different approach, Huisman et al. (2001) used changes in the traveltime of the direct groundwave in a wide angle reflection-refraction (WARR) survey to calculate lateral variations in wave velocity, which were subsequently transformed to near surface water content. While analysis of the groundwave has been shown to yield excellent results when the soil near the ground surface is approximately homogeneous, it is not clear whether accurate wave velocities can be obtained during an infiltration event. In this case, energy can be trapped in the low-velocity waveguide behind the wetting front. When the wetted zone has a

thickness similar to the radar wavelength, reflection multiples within this zone can interfere to produce dispersion in the groundwave (van der Kruk, 2006), which typically causes a diagnostic shingling appearance in the groundwave (van der Kruk et al, 2009). Whether accurate wave velocities can be estimated from the groundwave during infiltration events has therefore been queestioned (van der Kruk et al., 2009). In contrast, van Overmeeren et al. (1997) analyzed groundwave, reflected and refracted wave arrivals in multi-offset data obtained from central midpoint (CMP) surveys to successfully determine both lateral and vertical variations in water content, despite the fact that the characteristic shingling of van der Kruk et al. (2009) was apparent in the data.

Traditional multi-offset GPR survey techniques, i.e., CMP or WARR, are appealing strategies for monitoring water content changes associated with one-dimensional infiltration as they are well established in the literature (Berard and Maillol, 2007, Fisher et al., 1992, Greaves et al., 1996, Grote et al., 2005) and can be easily put into practice with widely available commercial GPR systems. Analysis of the data from these surveys typically relies on normal moveout (NMO) corrections (Fisher et al., 1992), however, which assumes idealized, locally continuous reflector geometries. To overcome these limitations, Bradford (2008) used reflection tomography to obtain improved velocity estimates and GPR reflection images in areas with significant lateral heterogeneity. The intensive surveying required to collect data for reflection tomography, however, makes the approach challenging to implement at the short time scales associated with the dynamics of individual soil hydrologic events, such as infiltration in response to rainfall. Given that natural infiltration in soils can often be

conceptualized as a one-dimensional process at field scales, it is not yet clear whether meaningful dynamic water content estimates can be obtained from multi-offset GPR using a NMO approach or whether more data intensive reflection tomography methods will need to be adopted.

There are relatively few examples in the literature that directly illustrate the influence of soil hydrology on surface-based GPR surveys (Freeland et al., 2006; Grasmueck et al. 2010, Grote et al., 2005, Haarder et al., 2011, Lambot et al., 2008, Moysey, 2010; Saintenoy et al., 2008; Truss et al., 2007). Truss et al. (2007) performed 3D time-lapse GPR imaging of infiltration in an oolitic limestone that revealed macroscopic funnel flow effects. These authors also observed overall shifts in reflector traveltimes that were suggested to be caused by changes in soil moisture, but they did not provide direct estimates of water content. Haarder et al. (2011) used constant-offset GPR surveys to monitor an infiltration experiment where dye was applied to mark preferential flow paths that were later identified when the site was excavated following the test. These authors concluded that wetting front non-uniformity and fingering complicated the GPR images noting impacts on both radar velocity and amplitudes, but preferential flow features themselves were not resolved. Grote et al. (2005) used constant-offset and CMP surveys to monitor changes in water content beneath a synthetic road bed during infiltration tests conducted over a period of approximately 35 weeks and found close agreement with gravimetric water content estimates. Moysey (2010) used a set of fixed antennas placed on the surface of a sand tank to show that changes in water content during wetting and drying events produce distinct arrival trajectories in transient constant

offset GPR data. These data were then used to calibrate the parameters of a soil infiltration model. Because the antennas were maintained at a constant offset from each other in that work, however, it was not possible to directly determine subsurface velocity or estimate reflector depths using the GPR data alone. Despite the various hydrologic and geophysical insights provided by these studies, none has directly evaluated whether multi-offset imaging can be used to quantify water content changes in a dynamically changing soil environment at timescales typical of rainfall and irrigation events.

In this study we investigate whether NMO analysis of WARR surveys can be used to continuously monitor water content, track infiltration fronts, and image soil structure over the course of a short-term infiltration experiment. The experiment is conducted in a sand tank where water is applied uniformly to the surface while an automated positioning system moves a receiver antenna to 21 different positions above the tank. This unique approach to antenna positioning allows us to collect multi-offset images as approximate 'snapshots' of the tank over time. Conceptualizing the data as a 3D volume, i.e., with dimensions of GPR traveltime, antenna offset, and elapsed time since the start of the experiment, provides a rich space for enhanced analysis of transient processes that we expect will allow us to achieve reliable, high resolution monitoring of hydrologic events in soils.

2.2. Methods

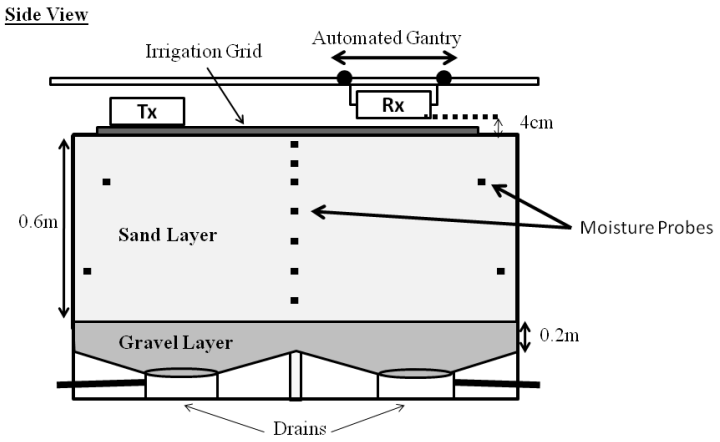

Figure 2.1: Experiment setup for lab-scale infiltration experiments.

2.1 Experimental Procedures

The infiltration experiment was conducted in a 150cm x 150cm x 80cm (LxWxH) wooden tank illustrated in Figure 2.1. Drains at the base of the tank were left open at all times to allow for free discharge of effluent. The tank was packed with a 60cm layer of homogeneous, medium grained (0.25-0.5mm) sand, below which was placed a 20cm layer of gravel to allow for drainage. While packing the sand, fifteen Decagon EC-5 soil moisture probes were installed in the tank. The probes were placed in a central array at depths of 5, 10, 15, 25, 35, 45 and 55cm and four lateral arrays, each with probes at depths of 15 and 45cm. The probes recorded water content at 10 second intervals throughout the experiment. The depth distribution of initial water content prior to the experiment was evaluated using the probes and found to be at equilibrium assuming no

vertical flow, though it was non-uniform due to redistribution of water during previous infiltration tests conducted in the tank (see Figure 2.2).

The infiltration event was initiated by applying water to the sand surface using an irrigation grid consisting of a network of parallel (0.64cm O.D. x 0.43cm I.D.) polyethylene tubes. The tubes were spaced at 1cm intervals and punctured every 1cm to give a 1cm x 1cm grid of irrigation points over the central portion of the tank (~130 cm x 75 cm) where the GPR data were collected. A peristaltic pump monitored by a flow meter provided control over the flux of water applied to the tank. The tubing was initially purged of air using a set of valves so that water could be applied uniformly to the surface of the tank as soon as the pump was turned on.

An automated radar imaging system was developed using LabVIEW (National Instruments, Austin, Texas) to achieve fast and accurate multi-offset antenna positioning for the WARR surveys performed during the experiment. A stationary transmitter antenna was placed on the irrigation grid 7cm from one end of the tank while the receiver antenna was mounted 4cm above the sand surface on a carriage that could move the length of the tank on an elevated track. The receiver antenna was moved using a belt drive (Pittman Express DC servo motor, Model GM9236S021-R1 and Pololu motor drive chip, Model MD01B), which had a 500 pulse per revolution encoder on the motor to provide lateral positioning precision on the order of tenths of a millimeter. LabVIEW was interfaced with the GPR trigger to fire the transmitter whenever the receiver antenna was stopped at a desired survey position, though the radar's standard control software was run from a separate computer to collect the data.

The radar system used in the experiment was a PulseEKKO 1000 with 900MHz antennas (Sensors and Software, Mississauga, Ontario, Canada). The transmitter antenna was fired at 21 different positions as the receiver was scanned across the tank with antenna offsets ranging from 0.44-0.9m. Each round trip of the receiver antenna across the tank was completed in approximately 60seconds, but data were collected in both directions so a complete 21 trace WARR survey was collected every 30seconds during the experiment.

No water was applied to the tank for the first 8 minutes of the experiment to ensure that consistent GPR data could be obtained and to assess background conditions in the sand. Water was then applied at the surface of the tank by the irrigation grid for 65minutes at a rate of 0.44cm/min; this rate was selected to provide a strong contrast in water content within the tank across the wetting front. After this time, the pump was turned off and an additional 107minutes of recovery data were collected as water redistributed in the tank. A total of 6300 GPR traces were collected as 300 multi-offset WARR surveys during the experiment.

2.2 Normal Moveout Analysis of WARR Surveys

Multi-offset GPR data are typically analyzed by applying normal moveout (NMO) corrections to determine the one dimensional velocity structure of the subsurface, e.g., see Yilmaz (1987) for details on NMO analysis and Fisher et al. (1992) for application of NMO to GPR. Using the NMO approach, the apparent (root mean square) velocity (V_{RMS}) of a wave traveling through the subsurface can be determined by assuming that the traveltime of a wave reflected from a subsurface interface increases in a

well-defined way as the offset between transmitter and receiver antennas is increased. For a horizontal interface, the relationship between the two-way traveltime (t) to a reflector located at depth (z) and antenna offset (x) is linear when plotted as x^2 vs. t^2:

$$t^2 = \frac{x^2}{V_{RMS}^2} + \frac{4z^2}{V_{RMS}^2} \tag{2.1}$$

The first step in NMO analysis of WARR data is therefore to identify a coherent set of arrivals in a multi-offset image that represent the reflection response from a subsurface interface. The traveltimes of the reflected wave estimated at each different offset between the transmitter and receiver antennas can then be fit by Eq. (2.1), with the resulting slope and intercept of the best fit line yielding V_{RMS} and the depth of the reflector. Due to the mode of data collection used in this study, identification of coherent reflections can also be aided by reflection patterns that are apparent when the data are plotted as constant-offset gathers as illustrated by Moysey (2010). We emphasize, however, that the ability to constrain both subsurface velocity and reflector depth over time is a key advantage of multi-offset versus constant-offset GPR data.

The effective dielectric constant (κ) of the subsurface can be determined from velocity given Eq. (2.2), where c is the speed of light in a vacuum. The dielectric constant can then be used to determine the average water content (θ) of the subsurface using a petrophysical equation such as the Topp equation (Topp et al., 1980), which is given in Eq. (3). For an in depth review and description of current GPR theory and applications refer to Jol (2009).

$$\kappa = \left(\frac{c}{V_{RMS}}\right)^2 \tag{2.2}$$

$$\theta = -0.053 + 0.029\kappa - 5.5x10^{-4}\kappa^2 + 4.3x10^{-6}\kappa^3 \quad (2.3)$$

2.3 Numerical Modeling

Numerical modeling of the infiltration experiment and GPR data was performed to improve the interpretation of the experimental results. Wetting and drying of the sand associated with the infiltration experiment were simulated using HYDRUS-1D (Simunek et al., 2005), which is a one dimensional finite difference model that solves Richards's equation for unsaturated flow. Soil parameters input into the HYDRUS-1D model were determined using laboratory hanging column tests and the van Genucthen soil model (van Genucthen, 1980). The 0.60m profile of sand was discretized into 1001 cells. Non-uniform initial soil moisture conditions were specified in the model based on the in-situ moisture probe readings observed at the beginning of the tank experiment (Figure 2.2). The same flux schedule used in the experiment was specified as the upper boundary condition in the model and the bottom boundary was specified as a seepage face to capture the capillary barrier effect that occurs at the sand-gravel interface in the tank. The hydraulic properties, determined from lab-scale hanging column experiments, used to represent the sand in the simulations are given in Table 2.1. The model was used to simulate the 180 minute duration of the experiment. Observation points were specified to represent probe locations in the tank, whereas the full simulated depth profiles were used to drive the model of the GPR response over the course of the experiment.

Table 2.1: Sand hydraulic parameters used in HYDRUS-1D simulations determined from multiple trials of hanging column experiments.

Residual Water content Θ_r [vol./vol.]	Saturated Water Content Θ_s [vol./vol.]	Air-entry Parameter α [cm^{-1}]	Shape Parameter n [-]	Saturated Hydraulic Conductivity K_s [cm/min]
0.06	0.38	0.058	4.09	4.6

The GPR simulations were performed using the finite difference time domain code implemented by Irving and Knight (2006) in MATLAB to solve Maxwell's equations in two dimensions. A cross-section of the true tank geometry parallel to the axis of the WARR surveys was used in the simulations. In addition to the sand, a layer of air outside the tank was also included in the model to allow for reflected and refracted waves at these boundaries to be captured within the simulations. Cell sizes for the entire model domain were optimized using the code and set to 0.05m x 0.025m (length x depth). Perfectly matched layer (PML) absorbing boundaries were specified around the model domain to eliminate additional spurious reflections. The vertical profile of dielectric permittivity for the sand within the tank was obtained by using the Topp equation, Eq. (2.3), to transform the water content profiles output from HYDRUS-1D. The electrical conductivity was set to constant values of $1nSm^{-1}$ and $0\mu Sm^{-1}$ for the sand and air, respectively. The conductivity of the sand was chosen to be constant since we are focused here on the kinematics of wave migration, but we acknowledge that changes in saturation would also affect the amplitude of the waves. The magnetic permeability was set to a constant value of $1.256*10^{-6}$ Henry/m (permittivity of free space). The source

wavelet used in the simulations was the normalized first derivative of the Blackman-Harris window with a dominant.

2.3. Results

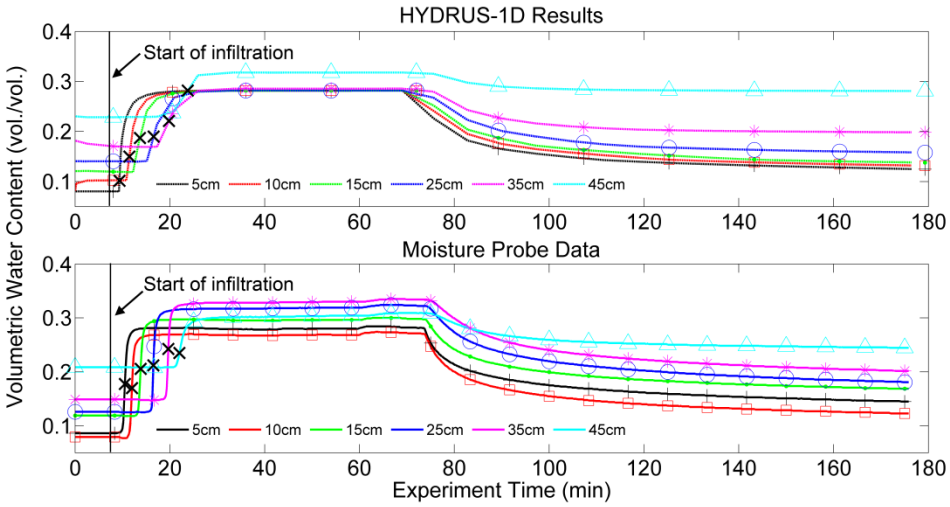

Figure 2.2: HYDRUS-1D model results and data from soil moisture probes located in the central array of the sand tank. "X's" indicate wetting front picks from taking the maximum of first derivative of the series in time. Solid vertical black line indicates start of infiltration.

2.3.1. Observations

Volumetric water content changes measured by the central array of embedded moisture probes over the course of the experiment are shown in Figure 2.2. Though the probes were calibrated prior to the experiment, one obvious inconsistency in the data is that the probe located at 0.10m depth is slightly drier than that at 0.05m. The shallower probe still responds first once infiltration begins, however, and the downward migration of the wetting front is apparent from the sequential increase in water content at each of the deeper probes as the experiment progresses; the arrival of the wetting front at each

probe is indicated by an x in Figure 2.2. The increase in initial water content with depth is responsible for the increasing velocity of the wetting front toward the bottom of the tank apparent in Figure 2.3. On average, however, the data shows the wetting front moves with an approximately constant velocity of 3.4cm min^{-1} in the upper 35cm of the tank. This velocity is generally consistent with the applied flux of 0.44cm min^{-1}, when the fact that the unsaturated fraction of the sand controlling the wetting front velocity ranges between about 10-20% (Figure 2.2). Data from the lateral arrays of probes installed at depths of 15 and 45cm (not shown) indicate that the migration of the wetting front was not completely uniform across the tank; at both depths the standard deviation of the front arrival time for the five probes in each array was 2.6 minutes. All probes reached constant water contents near 0.30 vol. $vol.^{-1}$ about 30 minutes into the experiment, indicating that steady state flow has been achieved. Subsequent drainage of the tank from top to bottom is also apparent in the probe data after irrigation was ceased 73 minutes into the experiment.

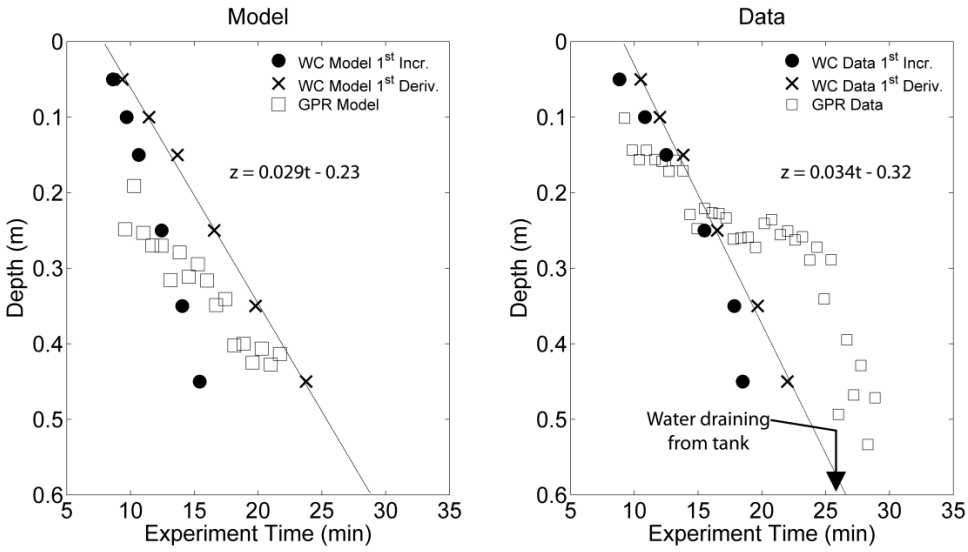

Figure 2.3: Estimated depth to the wetting front based on data from water content probes, GPR, and simulation results. Arrival of the wetting front in the data and HYDRUS model was calculated using the first arrival of water and the maximum temporal derivative. Water was observed draining from the tank at 26 minutes (indicated by the arrow).

Major arrivals that can be identified in the GPR data and model include the direct groundwave (A), a reflection from the bottom of the sand (B), reflection from the wetting front (C), reflection from the side of the tank (D), and the airwave (E) (Figure 2.4). Changes in the GPR arrivals during the experiment are shown for three representative times in the multi-offset images in Figure 2.5 and four representative antenna offsets in the constant offset images in Figure 2.6**.** Note that no processing other than dewow filtering and time zero correction has been performed on these data and plots were made with un-gained data.

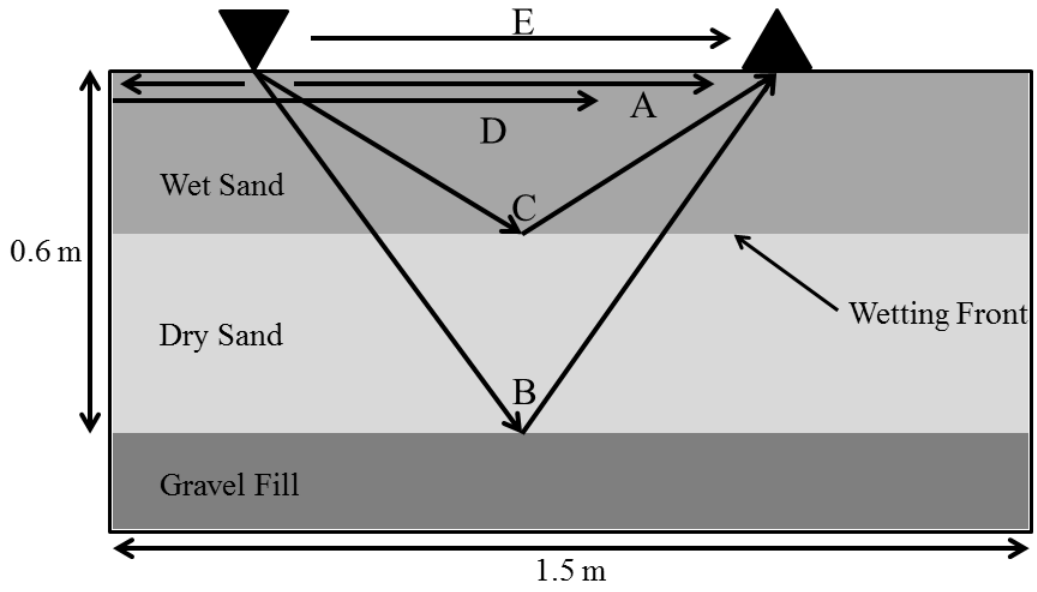

Figure 2.4: Raypaths for selected arrivals discussed in the paper. Arrivals shown here include the groundwave (A), bottom of sand reflection (B), wetting front reflection (C), side of tank reflection (D), and airwave (E).

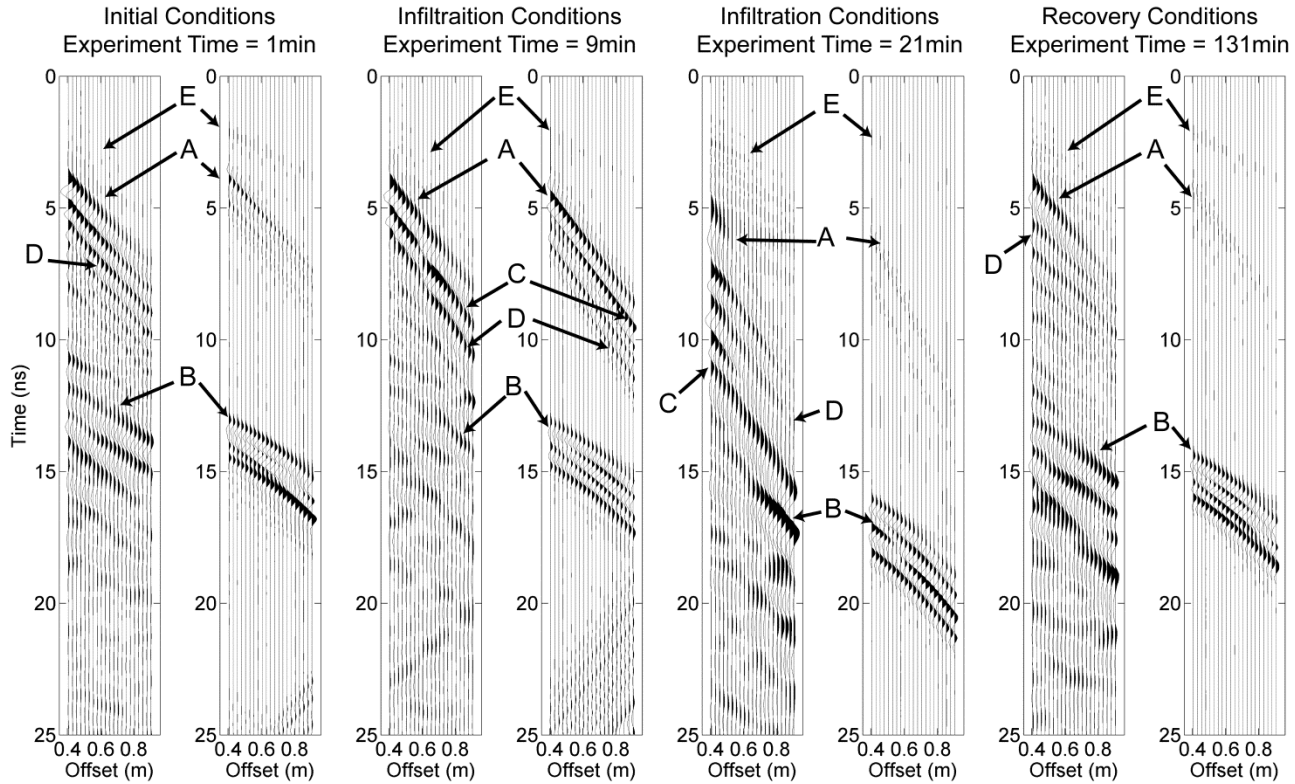

Figure 2.5: Multi-offset GPR sections at 1, 9, 21, and 131 minutes into the experiment are shown to represent initial, infiltration, and recovery conditions, respectively. For each time, data from the lab experiment are shown on the left and simulated data are shown on the right. Visible arrivals include the groundwave (A), bottom of sand reflection (B), the wetting front reflection (C), side of tank reflection (D), and airwave (E).

Although not used for the analysis in this study, we point out that the groundwave arrival (A) is difficult to identify at early experiment times due to interference from other arrivals, e.g. wetting front arrival. At later time, however, the groundwave is readily observed. There is also a loss of amplitude for the groundwave at large offsets and at all offsets the amplitude decreases during the period of irrigation, but rebounds slightly when the irrigation is terminated. While we have not evaluated the cause of these amplitude variations, they are consistent with changes in electrical conductivity associated with the varying water contents and interference between arrivals.

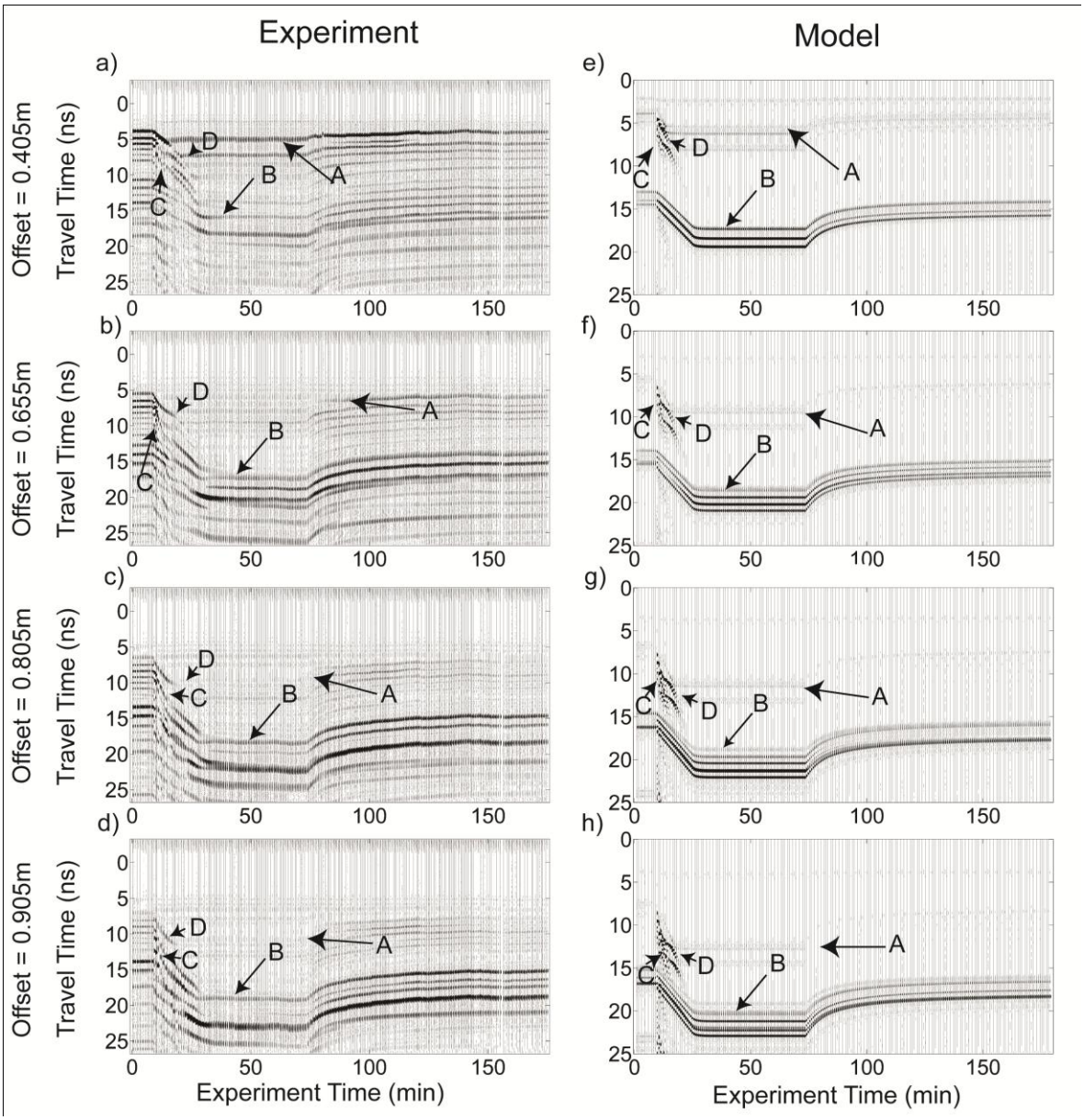

Figure 2.6: Common offset projections for 4 of the 21 offsets of the experiment and model. Pointed out in the data are the groundwave (A), bottom of sand reflection (B), wetting front reflection (C), and side of tank reflection (D).

The reflection produced by the bottom of the sand layer (B) can be clearly identified during the majority of the experiment, but it is obscured during the infiltration

period as the wetting front migrates downward (Figures 2.5, 2.6). A hyperbolic moveout of wave traveltime with antenna offset consistent with Eq. (2.1) can be seen in the multi-offset data, though interference is clearly apparent in Figure 2.5.3. For the constant offset images in Figure 2.6, the reflection pattern observed through time is similar to that observed for the moisture probe data, though it is inverted due to the inverse relationship between water content and wave velocity. Given that this reflection represents a fixed boundary in the tank, it is an important test target for evaluating whether soil heterogeneities can be used in the analysis of GPR monitoring data obtained during infiltration experiments.

Though it is more difficult to identify in the GPR data, arrival C indicates a reflection associated with the wetting front that marks the boundary between the water content perturbation caused by the infiltration event and the drier background conditions of the tank. The wetting front reflection is difficult to identify in the constant-offset data at early times (8-10min) due to interference with the groundwave (Figure 2.6). At later times in the experiment (15-20min) the wetting front arrival is still difficult to identify, though the cause of interference is hard to determine directly from the data. Numerical modeling results indicate that reflections from the walls of the tank (indicated as arrival D) contribute to the interference and the dry soil conditions ahead of the front allow for faster wave velocities in this region, which would be expected to produce refracted waves, though such arrivals were not readily identified in the data. A loss of reflection amplitude caused by decreasing contrasts in dielectric constant across the wetting front as the interface moves into the region of higher water content near the bottom of the tank is

also a factor. Lateral variability in the depth of the wetting front could be a third reason for difficulty in identifying a coherent reflection response in the multi-offset data given that variations in the propagation of the wetting front were observed across the tank with the moisture probes. It is difficult to directly infer the degree of lateral variability that occurred from the GPR data alone, however, given the single transmitter position used for the WARR survey in the experiment.

2.3.2. NMO Analysis of GPR Arrivals

The arrival most readily analyzed by NMO analysis is the reflection produced at the interface between the sand and gravel near the bottom of the tank. The changes in traveltime for this arrival over the course of the experiment are associated with variations in velocity caused by increases and decreases in the net volume of water stored in the sand. The reflection traveltimes picked from the multi-offset images were used with Eq. (2.1) to estimate the average (RMS) wave velocity within the tank throughout the duration of the experiment. The dielectric constant was then determined with Eq. (2.2) and water content values shown in Figure 2.7a were obtained from the Topp equation, Eq. (2.3).

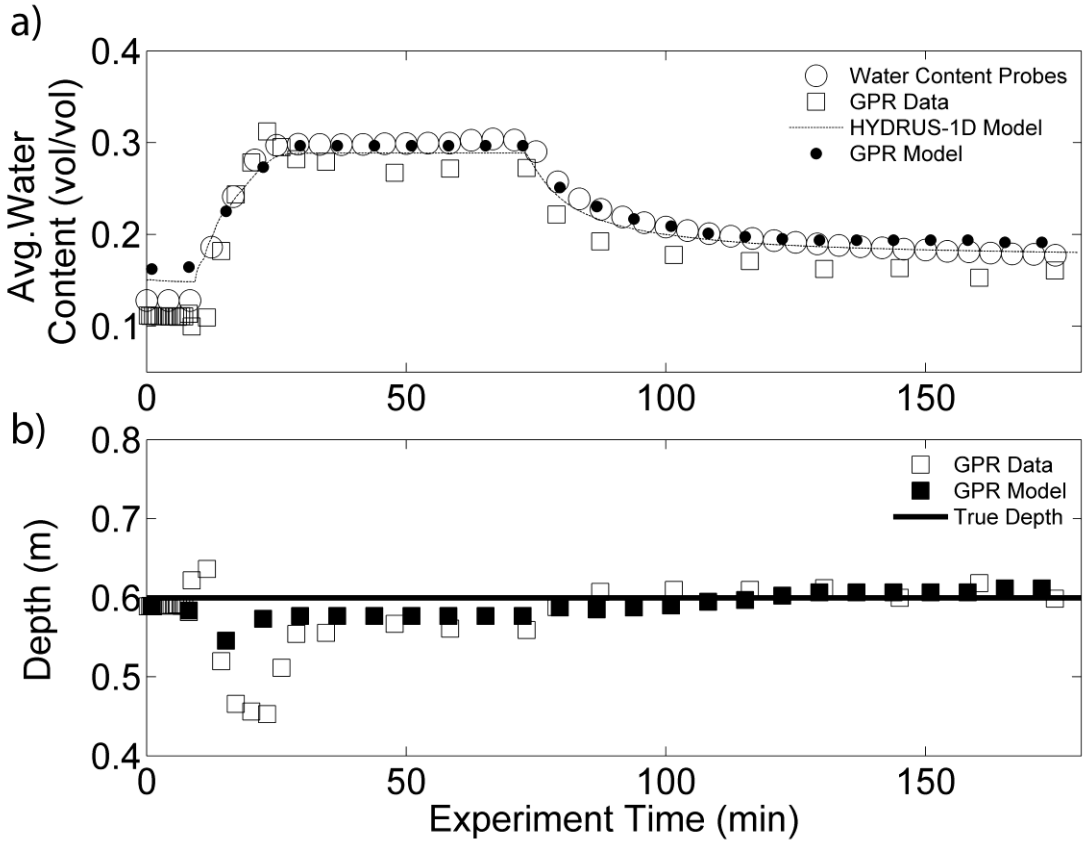

Figure 2.7: a) Average water content during the experiment estimated using the bottom of tank reflection in observed and simulated GPR data, moisture probes, and flow modeling with HYDRUS-1D. b) Depth to reflector estimated from bottom of tank reflection for both GPR data and model.

Despite the vertical variability of water content in the tank, Figure 2.7a shows that the trend in the depth-averaged water content estimated from the probes and that determined from velocity analysis of the reflection from the sand bottom are in reasonably good agreement. The GPR results generally underestimate the probe data by about 0.03 vol. vol.$^{-1}$, but not by a difference of more than 0.05 vol. vol.$^{-1}$. The numerical

modeling results, also shown in Figure 2.7a, similarly capture the overall patterns of depth-averaged water content in the tank derived from both the water contents simulated by HYDRUS-1D and NMO analysis of the synthetic GPR data. In contrast to the empirical data, it is notable that for the simulations the water contents derived from the NMO analysis overestimate the average water content. Given that the numerical simulations capture the interaction between the propagating waves and water content variations within the tank, this discrepancy implies that the water content errors are not associated with a general phenomenon such as preferential sampling of fast versus slow zones in the tank. Rather, the observed water content errors are more likely associated with a bias in picking the reflection arrival times in this particular experiment.

NMO analysis can also provide estimates for the depth to the interface causing the bottom of sand reflections, i.e., the thickness of the sand layer in the tank, which are shown in Figure 2.7b. The average depth to the bottom of the sand layer estimated over the course of the experiment is 58.7cm, which is a 2% error relative to the true sand thickness of 60.0cm. During the infiltration period, however, a significant amount of variation was observed in the estimates of the depth to the interface. Errors ranged from an underestimate of the interface depth of 15 cm (25% error) to an overestimate of 5cm (8% error). Although the errors are not as large for the analysis of the synthetic data, they are still most significant during the infiltration period implying that even under optimal conditions it can be challenging to obtain accurate depth estimates from GPR during highly dynamic subsurface events. While we emphasize that care should be taken

in interpretation of such results and that further research could lead to reduced errors, we note that for many practical purposes a reasonable estimate of interface depth can be achieved.

Despite the challenges in identifying the wetting front reflection discussed earlier, it is possible to approximately track this arrival in the GPR data by simultaneously considering arrival trajectories at multiple offsets. NMO analysis can then be used to estimate both the depth to and water content above the wetting front in the tank. The estimated EM wave velocity behind the wetting front is relatively constant over time with a value of 0.08-0.1m ns^{-1} in the wetted part of the tank. This range of velocity corresponds to water contents of 0.20-0.27 vol. $vol.^{-1}$, which is somewhat lower that the range of 0.26-0.34 vol. $vol.^{-1}$ observed with the moisture probes. The water content behind the wetting front estimated from the synthetic GPR data ranged between 0.18-0.21 vol. $vol.^{-1}$, which again underestimated the actual value of 0.22-0.28 vol. $vol.^{-1}$ obtained from HYDRUS-1D. Despite these errors in water content, Fig. 3 shows that the NMO analysis does fairly well in estimating the depth to the wetting front in the 1D model and the upper 25cm of the tank for the experimental data. Below 25cm on the experimental data, the trend of the NMO analysis seems consistent; however it is shifted forward in time by about 5minutes. Regardless, the overall downward trend of the wetting front is similar to that observed for the water content probes. Based on the GPR data the wetting front appears to reach the bottom of the sand layer in the tank between 25-30 minutes into the experiment (Figure 2.3), which is generally consistent with the time that water was observed to discharge from the tank drain 26 minutes into the experiment. The average

downward wetting front velocity estimated from the arrival time of the front reflection at the bottom of the tank is roughly 2.0-2.4cm min^{-1}, which is somewhat lower than but comparable to the rate calculated from the moisture probes (3.3cm min^{-1}). Overall, the analyses of the empirical and simulated data suggest that NMO analysis provides some insight about wetting front migration during an infiltration event, but falls short of providing accurate estimates of water content, front position, and velocity in this experiment.

2.4. Discussion

One of the key challenges identified in the NMO analysis was that wave interference between different GPR arrivals complicated estimation of reflection traveltimes from the data. In this experiment there are a number of arrivals other than the primary reflection from the wetting front and bottom of the sand layer that could have contributed to complexity in the observed data, including: 1) waves reflected from the wetting front or bottom of the tank that are subsequently refracted in the air at the surface of the tank, 2) reflection multiples within the wetting front, 3) refracted arrivals associated with high velocity zones ahead of the wetting front, 4) reflections from the side boundaries of the tank, and 5) reflections from the embedded moisture probes. We used the numerical simulations to aid in evaluating how arrivals 1-4 might have affected our interpretations of the hydrologic responses. Figure 2.8 illustrates the propagation of the radar waves as they interact with the tank for different hydrologic conditions before and during, the infiltration event; simulations during the recovery period are similar to those observed prior to infiltration.

As the reflection from the bottom of the tank returns to the tank surface an air refracted wave is generated. At large offsets this wave arrives slightly before the bottom of sand reflection causing a shorter apparent travel time giving higher apparent velocity in the tank, which translates into an underestimate for water content (Figure 2.7a). While this is consistent with the GPR data, this source of error remains inconclusive since the GPR model over estimates water content.

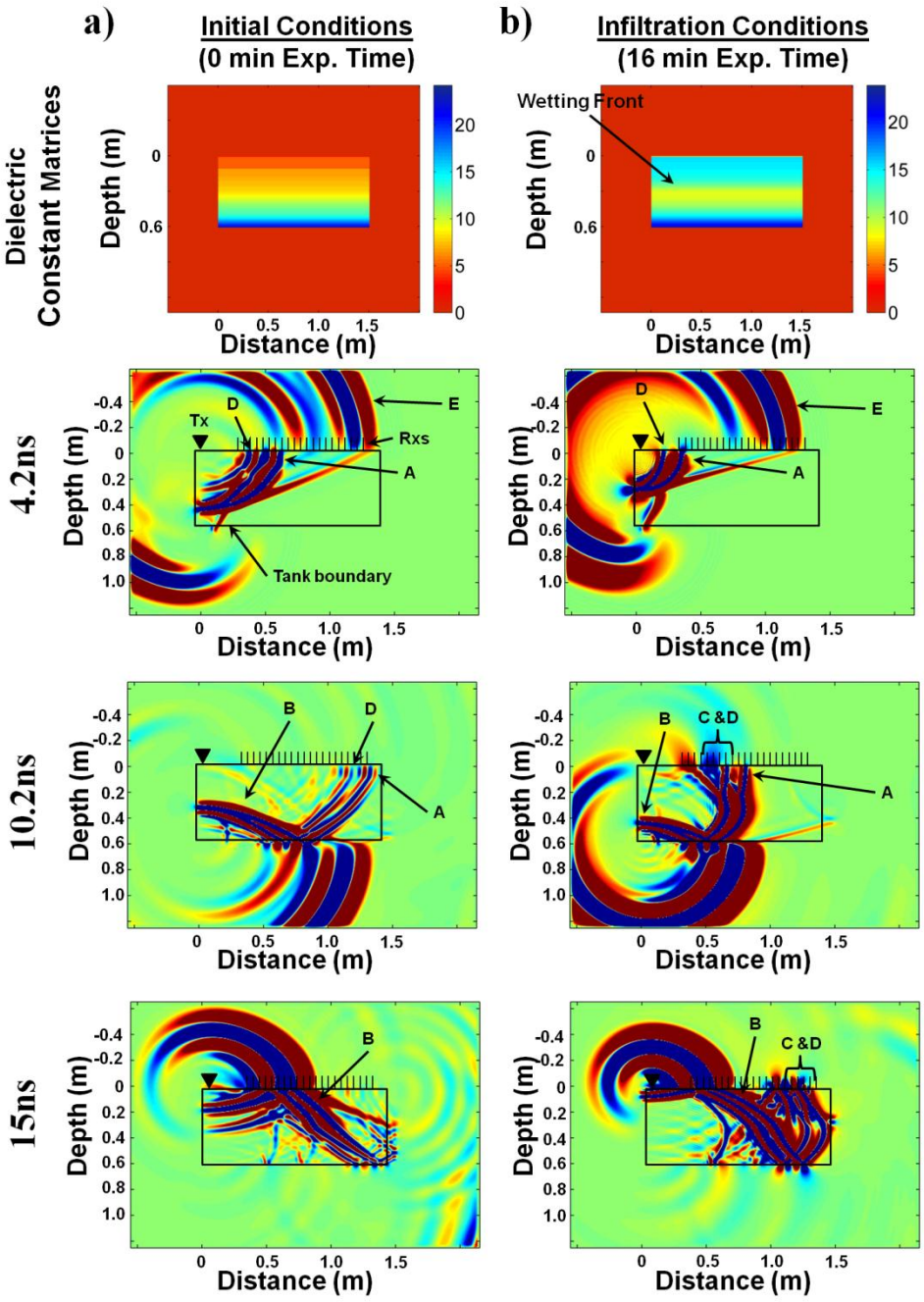

Figure 2.8: Propagation of radar waves during iterations of the 2D radar model showing evolution of radar wavefield through time for initial (t = 0 min) and infiltration conditions (t = 16 min).

The modeled wavefield is very complicated while the wetting front is propagating downward through the tank (Figure 2.8b). Evidence of multiple reflections from the wetting front can be seen in the simulations. These multiples do not appear to create the shingled appearance in the data suggested by van der Kruk et al. (2009) as an indicator for dispersive waves caused by the presence of a low velocity wave guide. This is likely due to the distance of the longest offset in our data (0.9m) being less than what is required to observe the shingling effect (van der Kruk, 2006). The shape of the groundwave is clearly affected at larger offsets, however, suggesting that dispersion is a factor in the data. Preliminary results (not shown) also indicate velocity dependent shifts in the frequency spectra of the groundwave at early infiltration time (8-10min) when the wetting front is very shallow (Figure 2.3), which is characteristic of dispersion due to the presence of a low-velocity waveguide (van der Kruk et al, 2009), i.e., the wetted zone behind the wetting front. This dispersive behavior implies that a standard traveltime analysis of the groundwave is not appropriate and requires that more detailed analysis that is sensitive to changes in the shape of the wavelet. This is one reason that we have chosen not to analyze the groundwave in this work.

It is also apparent from the simulation results in Figure 2.8b that the wave transmitted across the wetting front is refracted and begins to propagate ahead of the reflected waves, ultimately creating a head wave that interferes with the wetting front reflection. The impact of this interference is dependent on the depth of the wetting front. At early times in the experiment, when the thickness of the wetted layer is small, there could be sufficient separation between the arrivals to identify the refraction at large

receiver offsets. At later times in the experiment, when the wetting front is deeper in the tank, the arrivals would interfere with each other. Some of these effects may be present in our data, though from the constant-offset images in Figure 2.6 it appears that that a larger effect is the overall loss of reflection amplitude as the wetting front moves into wetter regions near the bottom of the tank due to lower dielectric contrasts. Overall, it is clear that complexities associated with dispersion and refraction caused by the wetting front make the analyses of the reflection from this interface complicated. We would have had extreme difficulty in identifying the wetting front reflection at all if not for the fact that we could use the 3D radar cube to simultaneously interpret transient responses from multiple offsets as the front propagated downward.

Reflections from the walls of the tank also complicate the data. For example, In Figures 2.8a, 2.8b, a secondary wave created by a reflection from the left wall of the tank follows the primary direct wave emitted by the transmitter. This scattered energy along with arrivals associated with the wetting front are likely reasons why we had difficulty in accurately estimating the depth of the tank during the period when infiltration was occurring (Figure 2.5). When simulations were performed where the tank boundaries were removed (results not shown), the wavefield becomes more coherent and easier to interpret. Also observed in the tank data was a reflection arising from one of the embedded soil moisture probes, which further added to the noise in the images. In general, however, the impact of these types of scattering could be reduced by migrating the GPR data.

Despite the fact that the NMO analysis used in this work was relatively simple, that our modeling assumption of a laterally-uniform wetting front is likely inaccurate based on the moisture probe data, and that there was substantial noise in the GPR data generated by scattering and refractions, we still obtained a good deal of quantitative insight into the macroscopic flow processes occurring in the tank using transient WARR surveys. It is possible that full 3D GPR imaging, where both the transmitter and receiver antennas are moved, could capture more details related to local variations in flow, i.e., non-uniformity of the wetting front or other preferential flow processes. For example, Truss et al. (2007) were able to capture the interaction between the wetting front and a meter-scale structural feature (sand-filled hole) that channeled flow during an experiment in the Miami Oolite. Both the 3D GPR monitoring studies by Truss et al. (2007) and Haarder et al. (2011) suggest, however, that directly capturing small-scale preferential flow features can be challenging. Haarder et al. (2011) were able to observe changes in reflection amplitudes that they interpreted to be caused by ponding associated with funnel flow, but they were not able to interpret individual small-scale preferential flow features directly from the GPR data. These authors concluded that GPR was useful for identifying patterns associated with large-scale flow processes, which have been observed by both Haarder et al. (2011) and Truss et al. (2007) to cause macroscopic changes in water content that produced shifts in the traveltime of reflections associated with soil heterogeneities. This is consistent with our results, where we have found that a reflection from a subsurface interface, i.e., the sand-gravel boundary at the bottom of the tank, could provide reliable estimates of average water content over time. The

complexity of the GPR response associated with the wetting front, the potential for preferential flow at scales below the resolution of GPR, and the quantitative consistency of water content estimates observed over both wetting and drying events in this study suggests that soil reflectors, i.e., physical contrasts in subsurface materials, are a critically important tool for quantitatively monitoring infiltration events.

Given that our experiment was intentionally designed to represent a simple soil environment with a single interface, it remains an open question whether our success in monitoring infiltration using the NMO approach could be achieved in more complicated environments. We acknowledge that acquiring more data, e.g., full-resolution 3D GPR surveys with multiple antenna offsets, will always hold more potential for resolving the details of infiltration in the subsurface. The time required to perform these surveys, however, is still a limiting factor; e.g., Truss et al. (2007) report that in their study it required 50 minutes to perform each constant offset survey over a 10m x 10m area using a custom single channel GPR that was integrated with an advanced positioning system specifically for 3D surveying. In contrast, multi-channel GPR systems amenable to fast WARR surveying over large areas are commercially available "off-the-shelf" at a reasonable cost. If NMO analysis of transient WARR data could be shown to provide reliable average water content estimates in heterogeneous soils, it would open a new opportunity to provide critically important data to hydrologists and soil scientists working at catchment scales.

2.5. Conclusions

A lab-scale infiltration and redistribution experiment was performed to constrain subsurface structures and water content variability with time. The unique form of automated transient multi-offset surveying used in this study allowed us to collect a 3D GPR data cube that can be viewed as either multi-offset or constant offset gathers. Normal move-out (NMO) analysis of reflections related to the bottom of a sand layer were used to independently estimate the mean radar velocity and average soil water content of the tank over the course of the experiment and provided agreement with averaged moisture probe measurements and numerical modeling results on the order of 0.03-0.05 vol. vol.$^{-1}$. It was also possible to independently determine the depth to the bottom of the sand layer with an average error of about 3% and maximum error on the order of 25%, which occurred as the infiltrating wetting front approached this interface.

The movement of the wetting front reflection was also visible in the GPR data. Analysis of this arrival allowed us to track the depth to the wetting front in the tank over the course of the experiment, which showed reasonably good agreement with moisture probe observations and modeling results obtained from the model HYDRUS-1D. The challenges in identifying this arrival are numerous, however, which illustrated the benefit of simultaneously using the multi-offset and constant offset gathers to interpret the wetting front response as a reflection surface within the 3D GPR data cube. Despite the fact that the moisture probe data indicated that the wetting front was non-uniform, we had a reasonable degree of success in capturing its behavior by assuming that it was laterally homogeneous. Further investigation is needed to more fully assess the errors of this one-

dimensional conceptualization and determine the additional value of collecting 3D GPR data to quantify non-uniform flow. There is also significant potential for learning about the early-time behavior of the wetting front by analyzing changes in the shape of the groundwave wavelet caused by interference between arrivals, such as reflection multiples within the wetted zone. Tools such as dispersion analysis (van der Kruk et al., 2006) and full-waveform inversion (e.g., Busch et al., 2010; Minet et al., 2010) are particularly promising for this purpose.

This study illustrates the potential of transient multi-offset reflection surveys for improving the characterization of vadose zone dynamics. The key advantage of the approach is that it is possible to estimate wave velocity and constrain the depth of subsurface structures directly from the GPR data without the need for supporting data, such as boreholes to independently constrain the depth to reflectors. Changes in water content can then be obtained if a petrophysical relationship between dielectric constant and water content can be estimated for the soil. Given that multi-offset data can be collected quickly in the field using commercially available equipment, the results of this study suggest that there is significant opportunity for non-invasive monitoring of soil moisture dynamics over catchment scales at time scales relevant to individual hydrologic events, if strong radar reflectors exist within the soil profile. Improved characterization of the hydrologic state of the subsurface at catchment scales will ultimately lead to a better understanding of vadose zone processes and advances in soil infiltration models.

3. Time-lapse GPR WARR surveying of heterogeneous vadose zone analogues during dynamic hydrologic conditions

Abstract

Three experiments were conducted to determine the transient multi-offset radar response during controlled irrigation events of 1) homogeneous sand, 2) a buried land mine in sand, and 3) a layer of silica flour embedded in sand. The homogeneous tank analysis from the previous chapter is used as a comparison tool to illustrate the effect of hydrologic state on GPR data interpretation. Hydrologic and GPR responses of the buried land mine are very similar to the homogeneous case; however, clear differences exist between the amplitude of early radar arrivals and are presented using amplitude vs. offset analysis. Strong amplitudes for the land mine at high water content values show potential for improved target identification if hydrologic state is considered in the data interpretation and analysis. The layered tank experiment also illustrated the importance of accounting for hydrologic state during GPR surveys as the GPR data resembled a single layer response at initial conditions, transitioning to a response dominated by layer reflection multiples at late times and high water content. In conclusion, analysis of WARR data indicated that homogeneous systems are easily interpreted for a range of hydrologic states, while more robust numerical signal processing algorithms may need to be employed for more complex cases. Despite errors in data analysis, the argument for using GPR to monitor dynamic vadose zone processes, e.g. infiltration, remains strong as

it provides a more robust and spatially resolved method for overall vadose zone characterization. These experiments illustrate the coupling of hydrology and GPR response in a simple way in order to provide a basis for monitoring dynamic vadose zone processes, e.g. infiltration, using GPR while developing a foundation for signal processing algorithms which will account for hydrologic state, providing greater accuracy for subsurface imaging.

3.1. Introduction

Identification of subsurface heterogeneities using ground-penetrating radar (GPR) outside the field of sedimentology have been the subject of relatively few studies, and are mostly limited to static hydrologic environments for archeological reconnaissance (Boniger and Tronicke, 2010, Bonomo et al., 2009, Rodrigues et al., 2009) and the location of buried pipes and tanks (Porsani et al., 2010, Zeng and McMechan, 1997). However, it is of particular concern to military applications in hopes of identifying hazardous unexploded ordinances (UXOs) (Al-Nuaimy et al. 2000, Gader et al., 2001, Ho et al., 2004, Wilson et al., 2007) through the use of pattern recognition algorithms.

It is well known that changes in EM wave behavior occur due to variability in water content of the background media (Topp et al. 1980, van der Kruk, 2006), which may degrade accuracy of GPR data analysis and result in an unidentified UXO. In general, Pettinelli et al. (2009) state that when compared to other methods, e.g. microwave tomography, basic studies are still required in order to improve target identification abilities of GPR. This paper takes the approach of Pettinelli et al. (2009)

and will illustrate that accounting for hydrologic state during GPR data interpretation is a step towards improved coherency of GPR data analysis.

Hydrologic state is determined by the quantification of volumetric water content. Water content is controlled on the pore scale by specific properties of the media (van Genuchten, 1980), e.g. hydraulic conductivity and porosity, while field scale water flow and distribution dependencies may be controlled by larger scale heterogeneities such as layers and lenses. Heterogeneities, such as differences in rock or sediment type, are known to affect fluid flow (Gerke and van Genuchten, 1993), however, even under relatively homogeneous conditions regarding soil type (Kung, 1990, Ritsema et al., 1993, Vervoort et al., 1999), heterogeneous distributions of water occur due to macropore structure, initial, and boundary conditions (Flury et al., 1994). This is especially important to the fate and transport of water and hazardous chemicals (Glass and Nicholl, 1996, Looney and Falta, 2000, McLay et al., 2001, Schapp and Leij, 2000, Stolte et al., 1994) and provides motivation for robust methods of vadose zone characterization such as surface based GPR.

The effect of hydrologic state on GPR data has been extensively studied by van der Kruk (2006) and van der Kruk et al. (2006, 2009, and 2010). This research focuses on errors in data inversion caused by dispersive properties of low-velocity waveguides caused by precipitation events. The dispersive properties of these waveguides are dependent upon the dielectric permittivity and thickness of the waveguide, as well as the dielectric permittivity of the layer below it. The dispersion of EM waves causes non-uniqueness in wave velocity determination and there for causes errors in GPR data

analysis. In these studies, wave dispersion was accounted for by determining the phase-velocity spectra, picking dispersion curves for the spectra, and inverting them to determine wave velocity. These studies clearly illustrate the importance of accounting for hydrologic state when analyzing GPR data.

Ground-penetrating radar (GPR) is well known to be capable of imaging subsurface structures (Best et al., 2003, Boll et al., 1996, Neal, 2004, Smith and Jol, 1992). It can also provide reliable estimates of volumetric water content at different resolution in time and space (Grote et al., 2010, Hubbard et al., 1997, Jonard et al., 2011, Lunt et al. 2005, Steelman and Endres, 2010) as well as imaging of wetting fronts from infiltrating water (Moysey, 2010, Vellidis et al., 1990); the premise of these hydrogeophysical studies, illustrated by Mangel et al. (2011), being that geophysical responses are highly dependent on water content of subsurface media.

Taking a step back from robust signal processing methods of the aforementioned GPR studies, this paper focuses on changes in the GPR response of geometrically simple subsurface environments for a range of hydrologic conditions. In order to illustrate changes in GPR response, transient multi-offset data was collected during controlled irrigation of water over a tank of homogeneous river sand for comparison to a landmine surrogate in a river sand background, to illustrate a discrete object response, and a thin layer of silica flour in a river sand background, to illustrate a continuous object response. During these controlled hydrologic perturbations, data is explored to analyze 1) if these heterogeneities are visible on wide-angle reflection refraction (WARR) data, 2) how these hydrologic and GPR responses differ from a homogeneous system, 3) if simple

analytical modeling is sufficient to analyze the GPR response, and 4) how signatures of these heterogeneities and overall GPR response change for different hydrologic states.

3.2. GPR Background

Time-domain surface-based GPR measures the time-dependent electromagnetic response of the subsurface to an incident wave of electromagnetic energy at a given central frequency. Wide-angle reflection refraction (WARR) surveys are performed by keeping one antenna stationary, in this case the transmitter, and stepping the other away at discrete position intervals (Figure 3.1), collecting data at each offset. Direct waves through the air (A) and ground (B) as well as refractions (D and E) have linear trajectories on multi-offset data while reflections follow a hyperbolic trajectory. For this specific survey geometry, reflected waves sample successive points along a reflector, separated by the step distance of the antenna. Reflections in the data are commonly correlated with stratigraphic boundaries (Neal, 2004), but can also arise from buried objects (pipes, tanks, UXOs, etc.) and infiltrating wetting fronts (Moysey, 2010). Typically, layered systems will produce reflections and refractions given contrasts in dielectric properties. Refractions are seldom seen in GPR data since EM wave velocity typically decreases with depth. However, in this research, refractions are highly anticipated as we are introducing water into the system, creating a low velocity layer above a higher velocity layer. All arrivals and their conceptualized EM wave raypaths and trajectories are outlined in Figure 3.1. The trajectories and coherency of these arrivals on multi-offset GPR data are crucial to qualitative interpretations and a

fundamental understanding of GPR data analysis. For a complete guide to GPR theory and analysis please refer to Jol (2009) or Annan (2003).

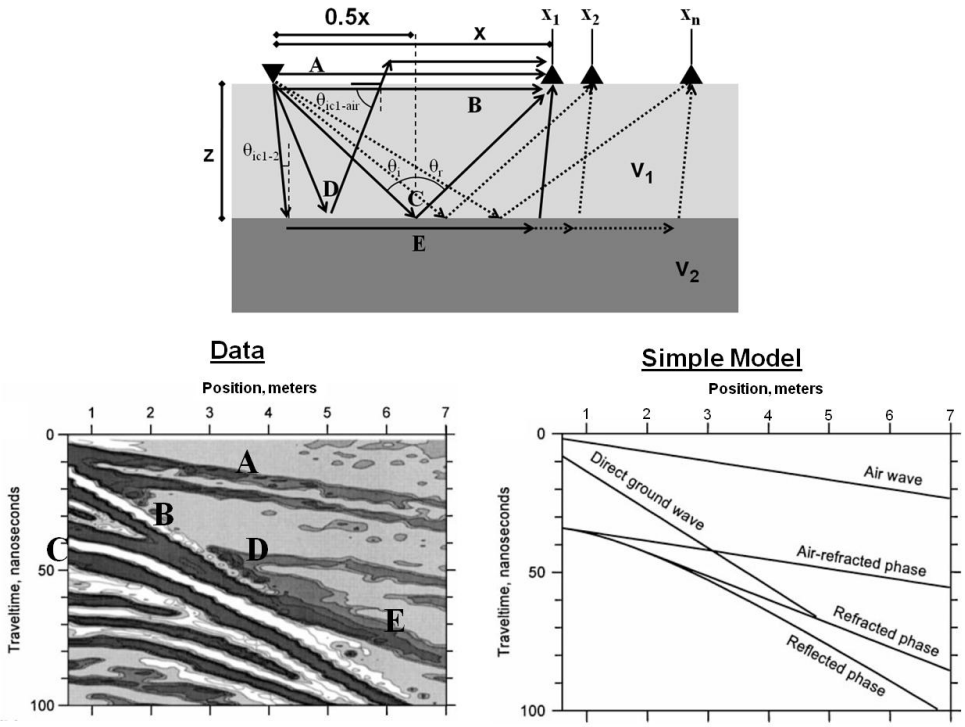

Figure 3.1: Schematic showing the raypaths, trends and locations of the airwave (A), the groundwave (B), the reflected wave (C), air refracted reflected wave (D) from the bottom and side of tank respectively, and layer refracted wave (E) on WARR data.

3.3. Experimental Methods

For all experiments, a PE1000 900MHz bistatic radar system was used (Sensors and Software, Mississauga, Ontario, Canada) in conjunction with an automated data acquisition system (Pittman Express DC servo motor, Model GM9236S021-R1 and Pololu motor drive chip, Model MD01B). This system was interfaced with a National Instruments data acquisition board (Model PCI-6225) and programmed in LabView

(National Instruments, Austin, Texas, USA). This unique setup allows data collection at multiple offsets through time through the use of a 500 pulse per revolution encoder with 0.01mm precision, producing a 3D data set with axes of experiment time, offset, and travel time. This unique data collection allows for multi-offset projections at discrete time intervals as well as common offset projections to track changes in arrivals with varying hydrologic conditions. These experiments were conducted in a 1.5m x 1.5m x 0.8m (L x W x H) tank (Figure3. 2), which is filled with 0.2m of gravel at the base and equipped with 4 drainages, each measuring 0.75 m x 0.75m.

Irrigation is controlled with a peristaltic pump and flow meter and distributed over $0.675m^2$ using a grid of 1cm x 1cm irrigation points constructed with parallel polyethylene tubing (0.64cm O.D. x 0.43cm I.D.). The grid is purged of air prior to experiments to ensure immediate irrigation upon powering of the pump. The transmitting antenna is located on the irrigation grid, centered at 0.75m on one side of the tank and 0.22m from the adjacent wall. The receiving antenna is suspended in the positioning system, raised 0.04m from the irrigation grid and positioned to collect WARR data at 21 offsets ranging from 0.405-0.905m collecting a complete data section in 30 seconds. All radar data is time-zero corrected, de-wowed, and gained using automatic gain control (AGC).

Table 3.1: Hydraulic parameters of test media.

Name	Residual Water content θ_r [vol./vol.]	Saturated Water Content θ_s [vol./vol.]	Air-entry Parameter α [cm^{-1}]	Shape Parameter n [-]	Saturated Hydraulic Conductivity K_s [cm/min]
River Sand	0.06	0.38	0.058	4.09	4.6
Silica Flour	0.005	0.41	0.22	1.62	4e-04

Hydraulic parameters determined from fitting data from water retention curves to the Van Genuchten model can be found in Table 3.1. Capacitance probes installed in three separate arrays and used for monitoring water content at 10 second intervals during the experiment were calibrated to the river sand using gravimetrically prepared samples at different water content values. The central array probes are named by their corresponding depth while the two lateral arrays are named by their depth and location (Figure 3.2). Initial conditions of the experiments, as measured by the capacitance probes, are assumed to be at equilibrium assuming no vertical flow, although the distribution of water is non-uniform from capillary forces and previously conducted experiments. General procedures for each experiment are essentially the same, however, location of probes, test media, flux schedules vary.

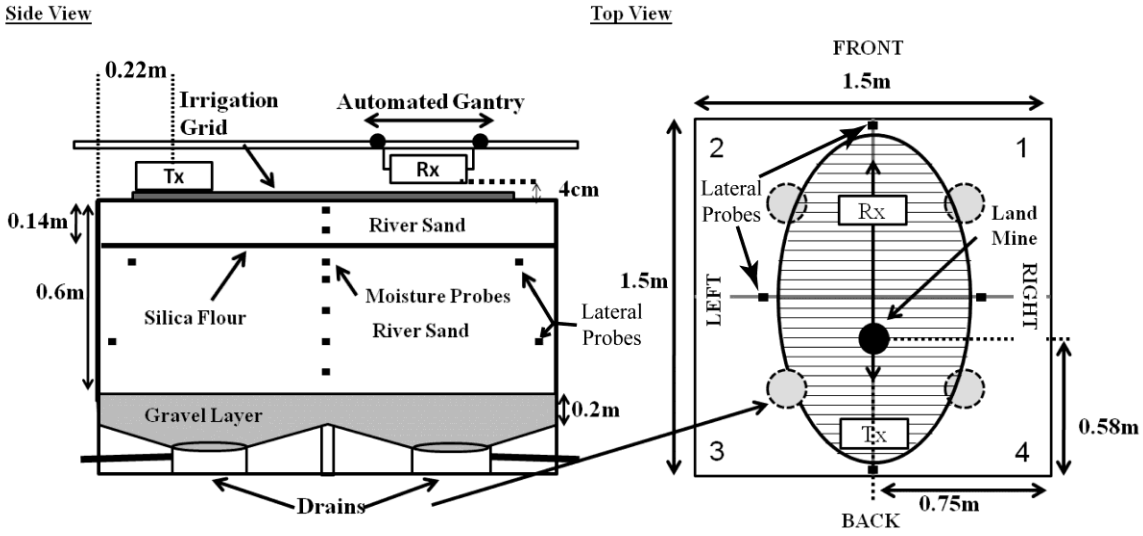

Figure 3.2: Experimental tank schematic showing silica flour layer (left) and the buried land mine (right).

3.3.1. Analytical Radar Modeling

For each experiment, a simple analytical model was developed using MATLAB software to establish if the simplest interpretation of the radar data was sufficient for data analysis. Velocities were plugged in to specific arrival traveltime equations in a guess and check fashion and resulting arrivals were plotted over the data to check for coherency with the data. Traveltime equations for direct, reflected, and refracted arrivals can be found in Burger et al. (2006). Specific arrivals for each experiment are outlined in their respective sections of this paper. For the homogeneous tank experiment, the model consisted of a single layer with a thickness of 0.60m. For the land mine surrogate experiment, the land mine was added as an object to the homogeneous tank. The layer experiment was represented as a two layer model with the first layer measuring 0.14m

and the second measuring 0.46m. Overall, this model provides insight into problems with data analysis while illustrating simple data interpretation techniques.

3.3.2 AVO Analysis

For the homogeneous and buried land mine surrogate experiments, amplitude vs. offset (AVO) relationships are derived for a window of data determined by calculating the trajectory of the groundwave. Radar wave velocities are calculated using the Topp Equation (Topp et al. 1980) to convert the average water content of the upper 0.15m of the tank, determined by averaging the water content readings of the 0.05m and 0.10m depth central moisture probes through time. Using these velocities, a trajectory for the groundwave was calculated and used to select a window of data to analyze the amplitude of the GPR response in the section of the data. Amplitudes in this window were squared and summed at each individual trace to give amplitude as a function of antenna offset and experiment time.

3.4. Homogeneous Tank Results

Medium-grained (0.25-0.55mm) river sand was packed in the tank to a depth of 0.6m. During the installation of the sand 15 Decagon EC-5 capacitance probes were installed in a central array at depths of (0.05, 0.1, 0.15, 0.25. 0.35,0.45, and 0.55)m along with two lateral arrays of four probes each at 0.15m and 0.45m located roughly 0.05 and 0.1m from the perimeter of the irrigation grid respectively. At the beginning of the experiment, the radar collected data for 8min to assess background conditions of the tank. At 8min, the tank received a flux of 0.44cm min^{-1} for 65min before it is terminated for

the remaining 107min of the experiment. A total of 300 WARR data sections were collected during the 180min experiment.

The hydrologic response, as measured by the in-situ capacitance probes, of the homogeneous tank is seen in Figure 3.3. A quick and consistently strong response from the central soil moisture probes at the onset of irrigation indicates that vertical flow is unrestricted. This is reflected in the radar data as a sharp increase in travel time for all arrivals (Figure 3.4b). All probes in the central array reached constant water contents ranging from 27-33% at 30 minutes into the experiment, providing evidence that steady-state conditions have been reached. Subsequent drainage of the tank from top to bottom is apparent in the central probe data after irrigation was ceased 73 minutes into the experiment.

Lateral probe arrays responded similarly with a decreased magnitude and increased period for the infiltration event. For example, the time required for the lateral array located at 0.20m depth to reach peak water content is lagged by 5-10min when compared to the central array, while the lateral array located at 0.45m depth never establishes a similar steady-state. Peak water content values for both lateral arrays are considerably lower than the central array, indicating that flow is dominantly one-dimensional, however, lateral spreading is observed 0.1m outside the perimeter of the irrigation grid at the lateral probe array at 0.45m depth. Water was observed steadily draining from the tank drains (Figure 3.2) in the following order: #4 and #1 (25min), #2 (26min), and #3 (28min). Variable magnitudes of water content at the moisture probes, and discrepancies between drainage times for the individual drains indicate a

heterogeneous distribution of water in the tank. Similar patterns associated with infiltration, steady state and drainage conditions are readily observed in the radar data (Figure 3.4b).

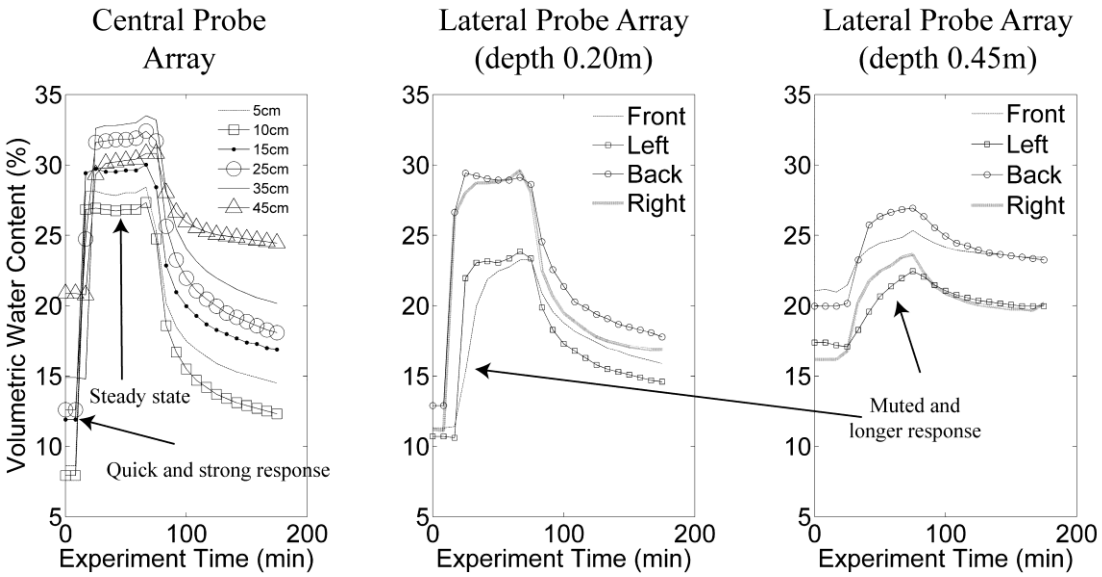

Figure 3.3: Hydrologic response of the homogeneous tank from the in-situ moisture probes.

Changes in the traveltime of radar arrivals seen throughout the experiment are caused by changes in the average water content of the tank (Figures 3.3 and 3.4). Using conceptualized ray paths to represent the propagation of EM waves (Figure 3.4a) we can determine what the radar data will look like, given a single layer model with thickness, *z*, and EM wave velocity v_{rms}. Expected arrivals (Figure 3.4a) for this experimental setup include the airwave (A), air refracted reflected wave from the side of the tank (B), groundwave (C), reflected wave from the bottom of the sand layer (D), layer refraction

(E), side of tank reflection (F), and air refracted reflection (G) from the base of the sand layer.

Multi-offset projections for initial, infiltration, steady-state, and recovery conditions, along with a common offset projection for the entire experiment time are seen in Figure 3.4. Coherency between the analytically modeled black lines for expected arrivals and the data are in good agreement. The airwave (A) and the groundwave (C) are visible on the data for the entire experiment (Figure 3.4b) and are easily identified with the analytical model. At 20min, the groundwave loses significant amplitude, and does not regain amplitude until the irrigation is terminated at 73min. The air refracted side of tank reflection (B) is not clearly visible on the data until the onset of irrigation as there is a considerable amount of interference prior to this; however, the onset of irrigation causes a downward shift of the groundwave, separating the two arrivals on the data (Figure 3.4c-f). The bottom of tank reflection (D) is strong and clearly identified by the analytical model for the entire experiment time, except during infiltration conditions (Figure 3.4d) where the arrival becomes obscured. After the onset of irrigation and at large offsets (>0.6m) the bottom of tank refraction (E) separates from the bottom of tank reflection (D), clearly visible in Figure 3.4e. The air refracted base of sand reflection (G) is very weak on the data, and likely would not have been identified without the usage of the analytical model. The conceptualization of this system as a single layer indicates that this system behaves as such, except during infiltration conditions. At this time, the system may be better represented as a two-layer system as the propagating wetting front causes a reflection and obscures the bottom of tank reflection.

NMO analysis for the bottom of tank and wetting front reflections was performed by Mangel et al. (2011) and is the subject of the prior chapter of this thesis. Overall, estimates of average tank water content and sand thickness were in good agreement for the entire experiment, except at times of infiltration were errors were on the order of 5% and 25% when compared to in-situ moisture probe data and the actual thickness of the sand, respectively. Depth to wetting front estimates also showed considerable differences when compared to moisture probes and HYDRUS-1D model results. It was concluded that wave interference caused errors in picking traveltimes for arrivals and resulted in errors in the NMO analysis. Assisting in the picking of these travel times, however, was the simultaneous viewing of common and multi-offset images. Regardless of errors in NMO analysis, it has been well illustrated in this paper that the occurrence and behavior of arrivals in the data is strongly dependent on hydrologic conditions. For more information about this experiment, please refer to the previous chapter of this thesis, or Mangel et al. (2011).

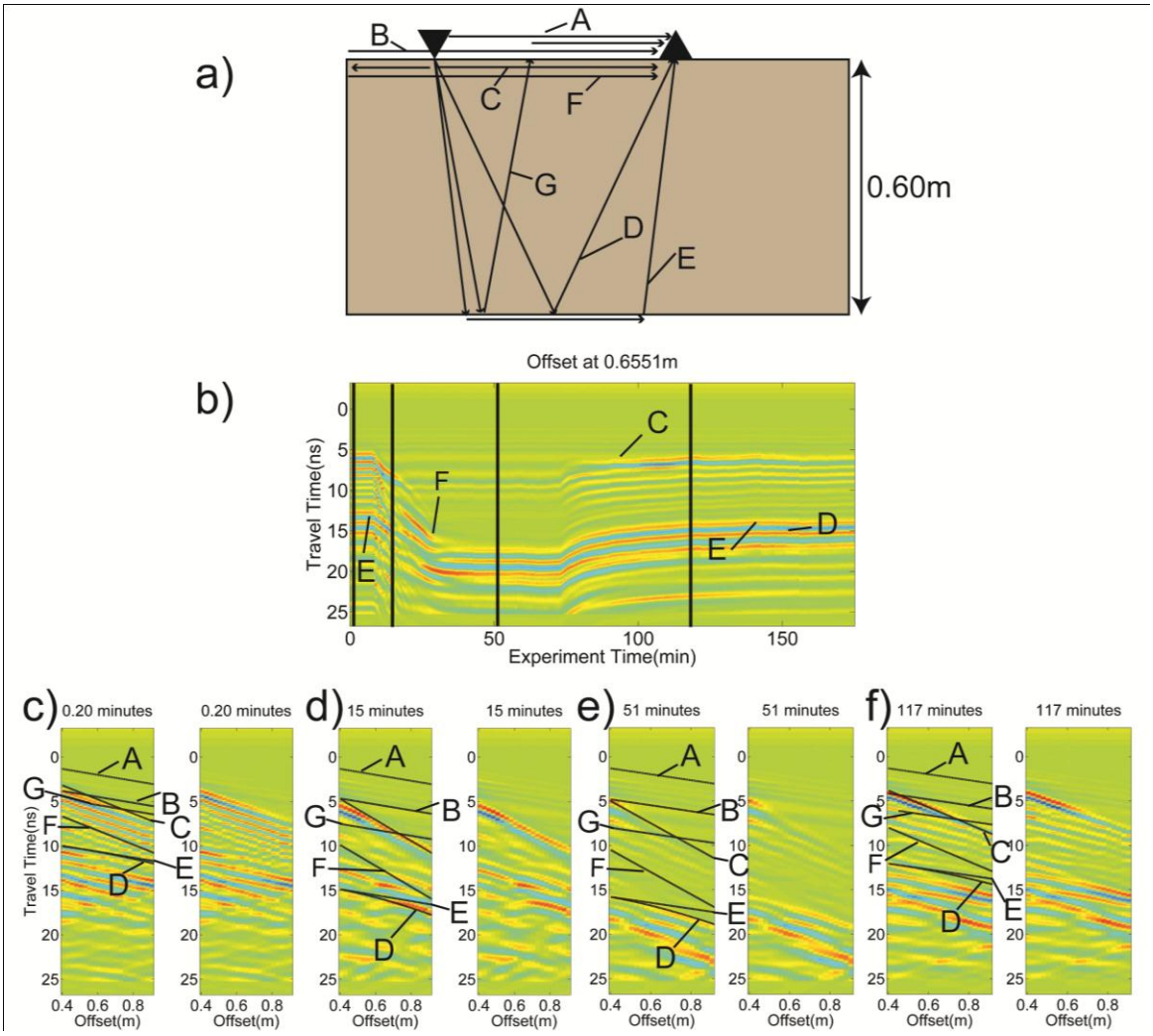

Figure 3.4: Conceptualized ray paths (a) and GPR response of the homogeneous tank for b) the entire experiment at a single offset, and at all offsets at discrete times, with and without model outputs (c-f). Model outputs include the airwave (A), the air refracted side of tank reflection (B), groundwave (C), the bottom of tank reflection (D), bottom of tank refraction (E), side of tank reflection (F) and air refracted base of tank reflection (G). Vertical black lines on (b) indicate times for (c-f).

3.5. Buried Land Mine Surrogate Results

An anti-personnel land mine surrogate (APNMC) was constructed with PVC sheet and pipe in accordance with instructions from Chant et al. (2005) with a diameter of 0.13m and length of 0.05m and buried so the top was at a depth of 0.05m. The center of the mine was located 0.75m away from the tank side wall and 0.58m from the wall where the transmitter is located (Figure 3.2) (Note: this is the only part of the volume of the tank that was disturbed after the homogeneous tank experiment). Homogeneous medium-grained river sand was used as the background media. Moisture probes were not disturbed from their original positions from the previous experiment. At the beginning of the experiment, the radar imaged the tank for 5 minutes to assess initial conditions of the tank. Irrigation was set to a flux of 0.3cm min^{-1} for 74minutes and terminated for the last 81minutes of the experiment. A total of 300 WARR data sections were collected during the 160minute experiment.

From the central array moisture probe data in Figure 3.5, it is clear that initially dry water content conditions at the central probes in the tank were quickly increased by the infiltration event, reaching a maximum of 25-32% for the central probes at all depths after 30min. The same increase is seen in both lateral probes arrays, although the response is decreased in amplitude and increased in period with depth, indicating the lateral spreading of water from the central distribution area of the grid (Figure 3.2). As seen in the homogeneous experiment, the data for the lateral probes at 0.15m depth reach a constant water content indicating steady state which is lagged behind the central probes by 10min while the data from lateral probes at 0.45m depth never exhibit a similar

pattern. Water was observed draining from the tank drains (Figure 3.2) in the following order: #1&4(28min), #2(33min), and #3(35min). The hydrologic response of this experiment is nearly identical to the response of the homogeneous tank experiment with the exception of slightly lower maximum water content values, due to the lower applied flux rate. Regardless of a similar hydrologic response, the geophysical response shows key differences when compared to the homogeneous experiment.

A similar trend in GPR arrivals when compared to the homogeneous experiment is readily observed in Figure 3.6b, with a sharp increase in traveltimes, followed by a constant section and a subsequent decrease in travel time associated with the changes in average water content of the tank. Similar arrivals are expected here as with the homogeneous tank with the addition of the land mine reflection and air refracted land mine reflection. Modeled arrivals (see Figure 3.6a) include the airwave (A), air refracted side of tank reflection (B), groundwave (C), bottom of tank reflection (D), bottom of tank refraction (E), air refracted mine reflection (F), mine reflection (G), side of tank reflection (H) and air refracted base of tank reflection (J).

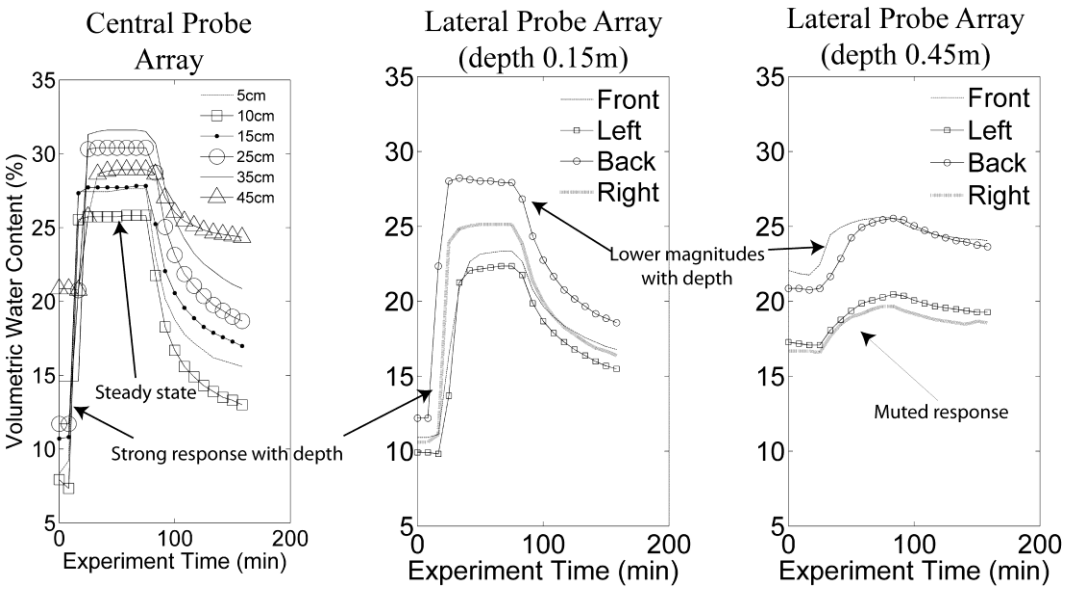

Figure 3.5: Hydrologic response of the tank with a buried land mine from the in-situ moisture probes.

Multi-offset projections for initial, infiltration, steady-state, and recovery conditions, along with a common offset projection for the entire experiment time are seen in Figure 3.6b-f. The analytical model performs well once again for the identification of the airwave, groundwave, air refracted side of tank reflection and bottom of tank reflection arrivals with some discrepancy during infiltration conditions for the bottom of tank reflection. All these arrivals exhibit a similar behavior as seen in the homogeneous tank experiment with slight differences in patterns arising from differences in the applied flux schedule.

The land mine response as measured by the reflection (G) is unclear as there is a considerable amount of interference with adjacent arrivals for the duration of the experiment (e.g. groundwave and side of tank reflection). In order to evaluate this arrival

and attempt to quantify changes in the GPR response of the land mine for hydrologically variable conditions, we compare it to similar conditions using the homogeneous tank experiment using amplitude vs. offset (AVO) relationships.

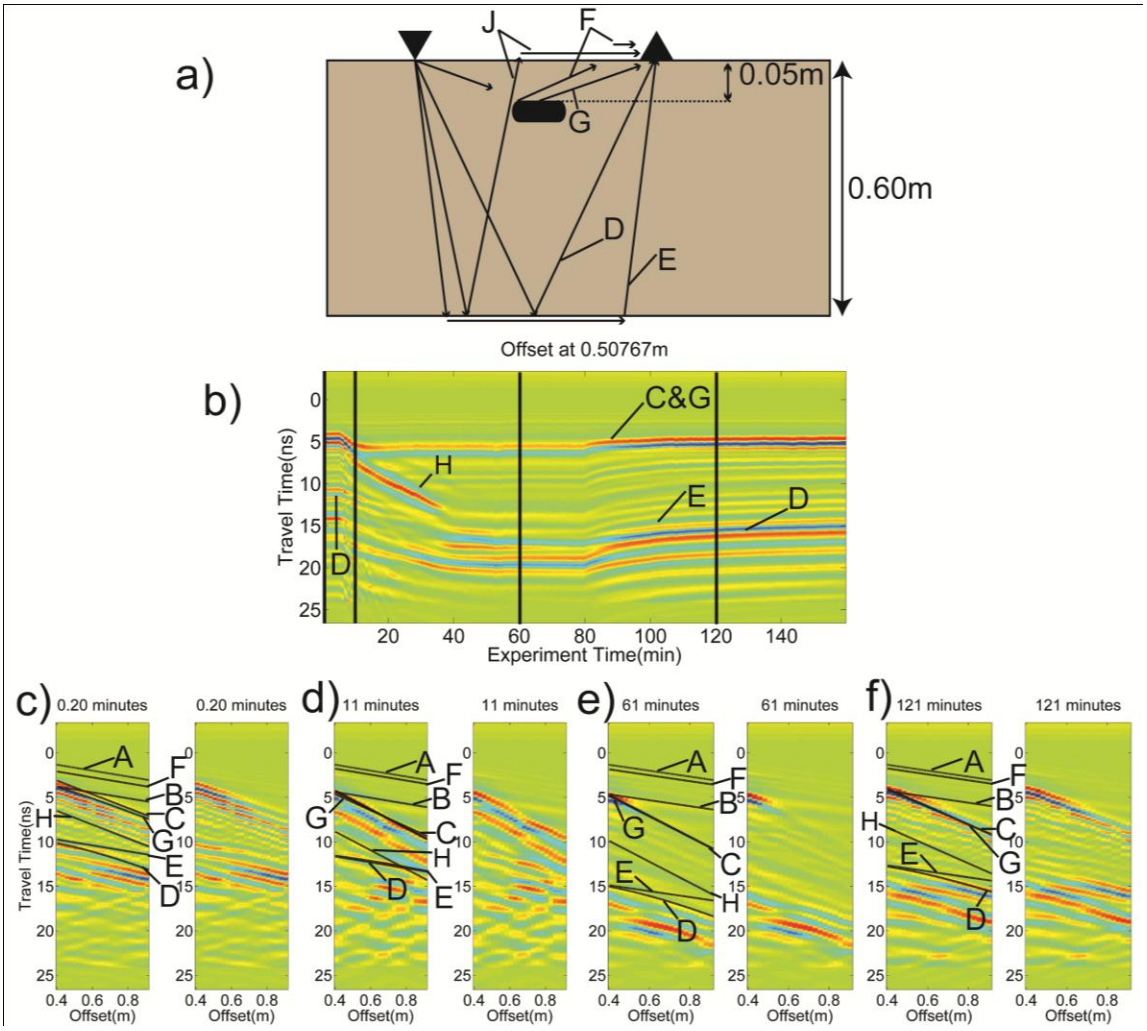

Figure 3.6: Conceptualized ray paths (a) and GPR response of the tank with buried land mine for b) the entire experiment at a single offset, and at all offsets at discrete times (c-f) showing the airwave (A), air refracted side of tank reflection (B), groundwave (C), bottom of tank reflection (D), bottom of tank refraction (E), air refracted mine reflection (F), mine reflection (G), side of tank reflection (H) and air refracted base of tank reflection (J). Vertical black lines on (b) indicate times for (c-f). Omitted raypaths for A, B, C, H are identical to those in Figure 3.4a.

Comparing Figures 3.4e and 3.6e side by side, there is a noticeably higher amplitude arrival at shorter offsets (<0.6m) for the land mine experiment. In the homogeneous tank experiment, this experiment time was characterized by steady-state hydrologic conditions and weak groundwave amplitudes, likely due to the high water content of the upper part of the sand. This is not the case in the land mine experiment as similar hydrologic conditions exhibit a different GPR response due to a physical heterogeneity in the subsurface. To compare these two responses we employ coarse estimates of AVO relationships, as outlined in section 3.3.2, to illustrate the differences between the two experiments as well as changes in response due to hydrologic state.

Considerable differences in the sum of squared amplitudes are observed for the duration of the experiments in Figure 3.7. Peaks in amplitude of this data window are similar for the onset of irrigation for both experiments associated with the development of the wetting front. Given similar hydrologic conditions, as quantified by average water content, the amplitude for the land mine experiment at this time is four orders of magnitude greater than the homogeneous experiment, indicating that AVO relationships will offer significant insight into the identification of buried objects. Figure 3.7 also indicates that increasing water content values to eliminate groundwave amplitude may provide better conditions for identifying shallow buried objects as it will minimize the interference between the arrivals.. It is also noteworthy that subtle changes in amplitude due to changes in hydrologic state are observed for the land mine experiment, but may be the effect of groundwave attenuation, as the groundwave is included in this analysis.

Overall, the coupled hydrologic and GPR responses for this experiment are relatively simple as the hydrologic response was nearly identical to the homogenous case and the conceptual radar model was able to track changes in GPR arrivals well. Viewing the data as both common and multi-offset images is extremely helpful in basic data interpretation, while AVO relationships offered clear evidence that GPR response is dependent on hydrologic conditions. This illustrates the appeal of monitoring dynamic hydrologic environments with GPR and provides motivation for further development of signal processing algorithms to assess AVO vs. hydrologic state relationships to increase accuracy of AVO pattern recognition.

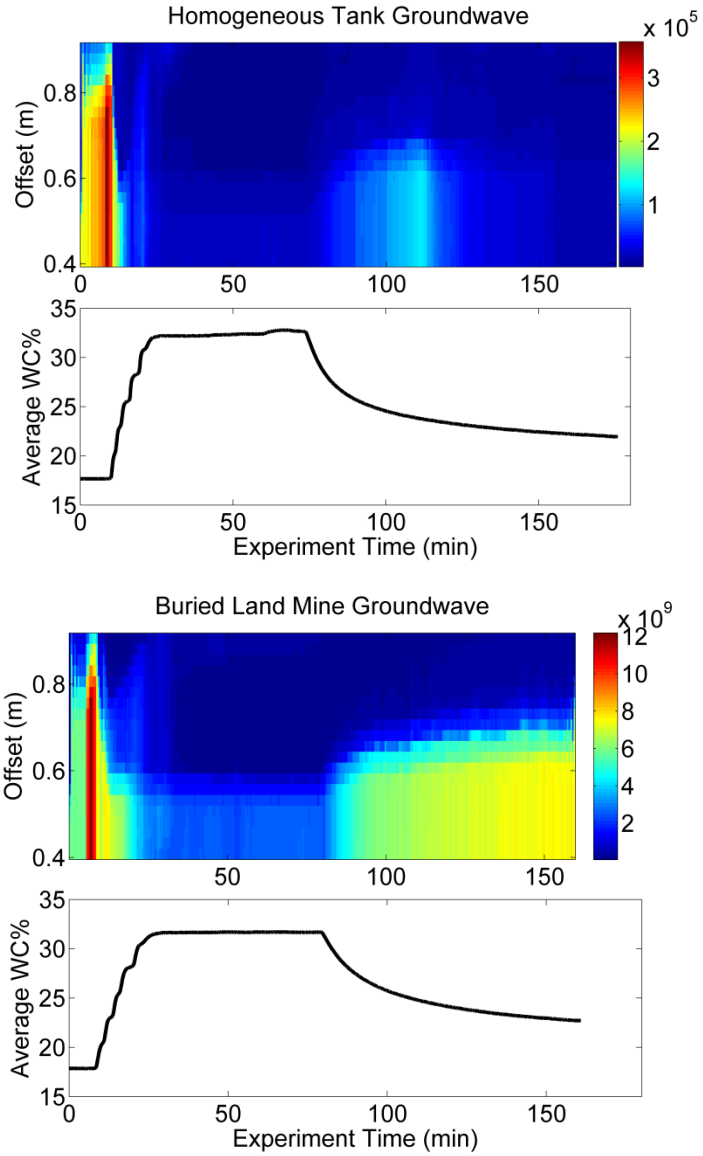

Figure 3.7: Amplitude vs. offset relationships for homogeneous tank and buried land mine groundwave trajectories illustrating differences in amplitude occurring from the presence of the land mine surrogate at similar hydrologic states.

3.6. Layered Tank Results

A thin (1cm) layer of silica flour was installed after the medium-grained river sand from the previous homogeneous tank experiments was excavated to a depth of 0.15m. A permeable garden fabric was used to line either side of the layer of silica flour in order to prevent mixing of the two medium and to provide a sharp boundary. Lateral and central moisture probes previously located at 0.15m depth were moved below the layer to identical locations at 0.20m depth to capture breakthrough times of water moving through the layer. Probes below 0.20m remained undisturbed and central probes above the layer were re-installed at 0.05 and 0.10m depth. After adding the layer, the excavated sand was replaced. At the beginning of the experiment, the radar imaged the tank for 5 minutes to assess initial conditions of the tank. The irrigation flux was set to 0.3cm min^{-1} for 135 minutes, then increased to 0.44cm min^{-1} for 20minutes, and terminated for the last 49 minutes of the experiment. A total of 400 WARR data sections were collected during the 204 minute experiment.

In this case, both hydrologic and GPR responses are significantly different from the homogeneous experiment. It is clear from the moisture probe data in Figure 3.8, that water flow is inhibited between 0.10-0.20m as central array probes at 0.05 and 0.1m responded immediately to the onset of irrigation at 5min, while central probes located deeper than 0.1m remain at initial conditions until 140min. The 0.05m and 0.10m central probes increased to values at late experiment times (>100min) of 50% and 45% respectively. This reading is abnormally high considering the porosity of the sand is 0.38, indicating that positive head has been established in the upper layer of the tank and

flow is no longer 1D and vertically dominated as observed in the two previous experiments.

Lateral moisture probes exhibited a similar behavior as the lower central probes, responding late in the experiment (around 140min) with variable magnitudes, not exceeding 15% and 25% at the 0.20m and 0.45m lateral arrays respectively. The back moisture probe in the 0.20m depth lateral array (see Figure 3.2), along with the central probe at 0.25m, did not respond. This lack of response is attributed to the water flowing around this volume of the tank due to heterogeneous distribution of water above the layer. Water was observed intermittently draining at the #2 and #3 drains (Figure 3.2) around 75min into the experiment while steady drainage from each drain occurred in the following order; #4 (178min), #1 (179min), #2&3 (187min). This drastic change in hydrology when compared with the previous experiments resulted in a significantly different GPR response (Figure 3.9).

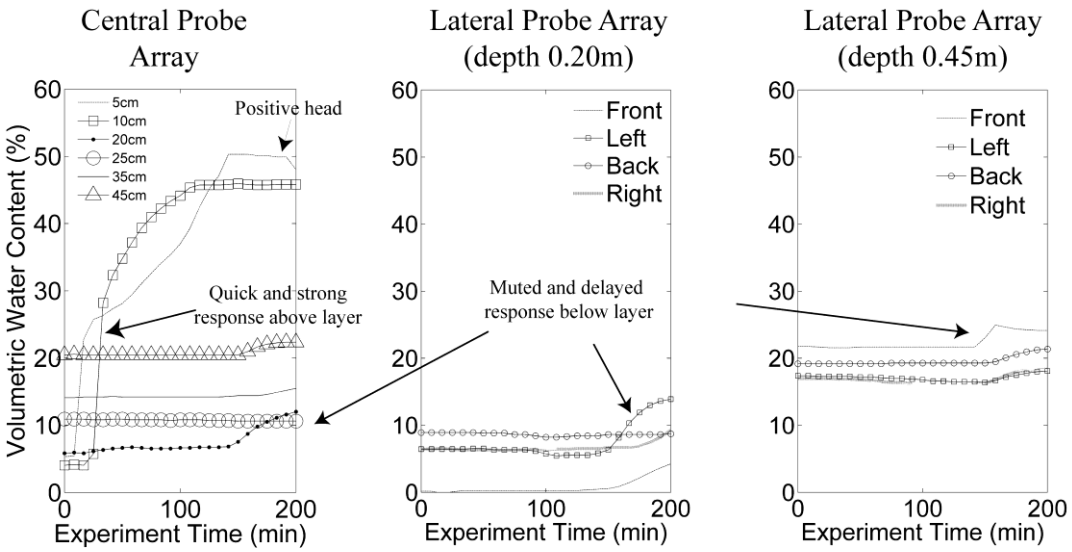

Figure 3.8: Hydrologic response of the layered tank from the in-situ moisture probes.

A two-layer analytical model was used to delineate possible sources arrivals and determine if the conceptualized response is reflected in the data. Modeled arrivals (Figure 3.9a) included the airwave (A), air refracted layer reflection (B), air refracted side of tank reflection (C), groundwave (D), layer reflection and multiple (E, 2E), layer refraction (F), bottom of tank reflection (G), bottom of tank refraction (H), and side of tank reflection (J).

Multi-offset projections for initial, infiltration, first water (75min), and fully saturated conditions, along with a common offset projection for the entire experiment time are shown in Figure 3.9. At initial conditions, the model shows good agreement with the airwave, groundwave, air refracted side of tank reflection, layer reflection, bottom of tank reflection, and bottom of tank refraction. However, it is unclear whether the layer reflection is actually present on the data, since the thickness of the layer (1cm)

is below the expected resolution of the radar system (3.3cm). During infiltration conditions, it is also unclear as to whether this arrival is arising from the layer itself, or the propagating wetting front moving through the upper layer. At these early experiment times, there is significant interference between the groundwave and layer reflection. Almost immediately after irrigation begins at 5min, the bottom of tank reflection (G) is no longer visible on the data, however, may be coincident with the side of tank reflection (J) at late experiment times (Figure 3.9f). At 50min experiment time the layer reflection is clearly identified as the groundwave is no longer coincident. As water content increases in the upper layer, arrivals associated with this layer, e.g. groundwave and layer reflection (plus multiple), continue to increase in travel time causing severe interference with the bottom of tank reflection and refraction. At late experiment times (Figure 3.9f) between 75-180min, a very weak amplitude layer multiple (2E) is observed. This fairly simple system is clearly not as well represented with the simple analytical model as was the case with the two previous experiments. The airwave, groundwave, air refracted side of tank reflection, layer reflection, and layer multiples seem to be captured well by the model, however, other more complex arrivals are difficult to identify using this method, providing evidence that GPR response is dependent on hydrologic state, and more robust methods of data analysis will need to be employed.

Overall the GPR response of this experiment is fairly complicated. However, the complexity of this response is significantly reduced by the data acquisition process; allowing simultaneous viewing of multi-offset and common offset images. At early times, the response of this system is as expected, although uncertainties about the cause

of the layer reflection remain unclear. At late times in the experiment, the data interpretation process becomes convoluted using the analytical model, and leaves room for more advanced signal processing algorithms. 3D modeling of this system will likely need to be employed in order to comprehend the hydrologic and GPR response due to the heterogeneous distribution of water above the layer and subsequent unstable flow.

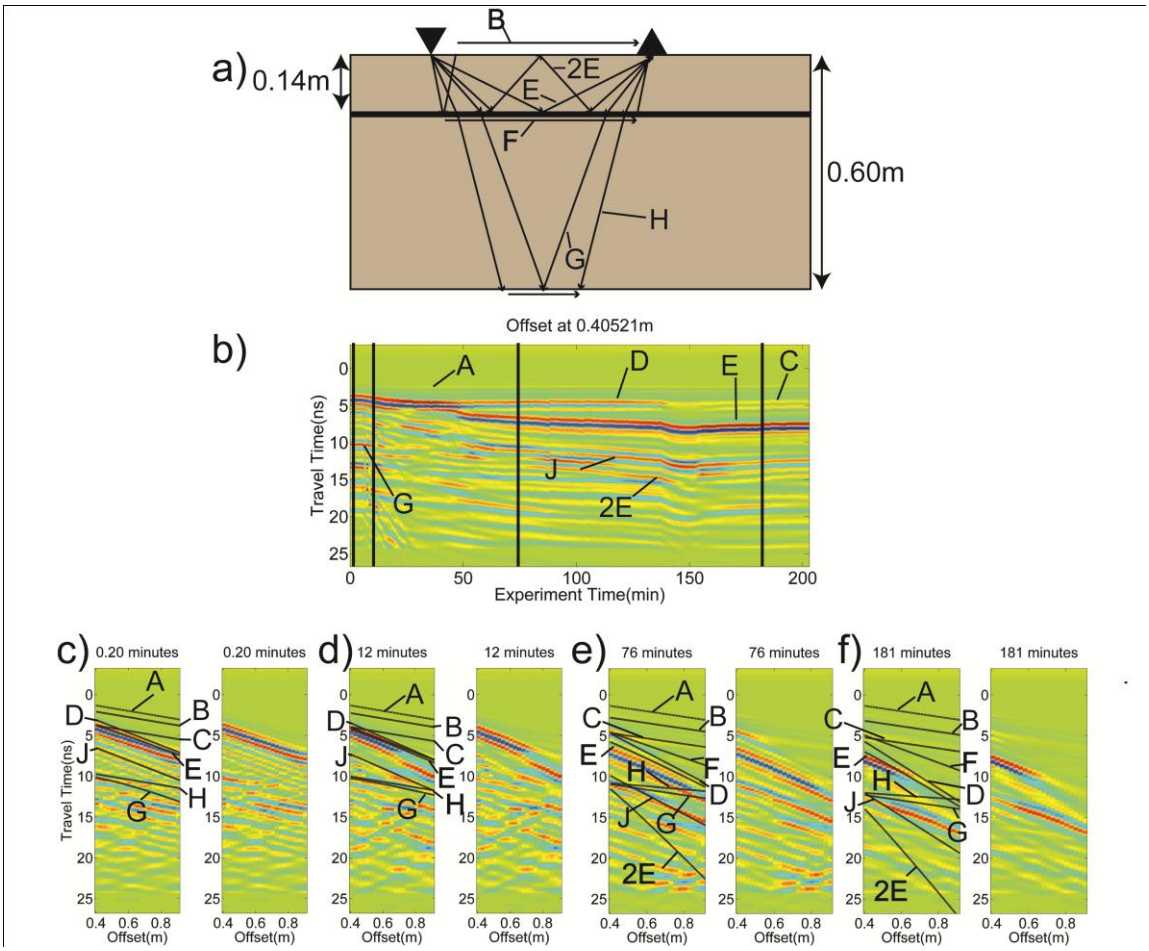

Figure 3.9: GPR response of the layered tank for a) the entire experiment with antenna offset = 0.405m, and all offsets at b) initial conditions, c) infiltration conditions, d) first sign of tank drainage, and e) saturated conditions. Shown here are the airwave (A), the air refracted reflection from the layer (B), air refracted reflection from the side of the tank (C), the groundwave (D), layer reflection and multiple (E, 2E), layer refraction (F) bottom of tank reflection (G) and bottom of tank refraction (H). Vertical black lines on (a) indicate times for (b-e).

3.7. Discussion

This dependency of data accuracy on hydrologic state was readily observed in the homogeneous experiment during infiltration conditions for the bottom of tank reflection (D), and throughout the experiment for the bottom of tank refraction (E) (Figure 3.4). During infiltration, the bottom of tank reflection became incoherent and hard to analyze on the images due to an additional reflection caused by the propagating wetting front (C). This effect resulted in relatively high errors from the NMO analysis of this reflection, corresponding to a 5% error in water content and a 25% error in depth measurements, caused by errors in traveltime picks. Errors in the NMO analysis were also attributed to the bottom of tank refraction arrival causing errors in picking of the bottom of tank reflection (Figure 3.4c-f). As average water content in the tank increases from Figure 3.4c-e, the bottom of tank refraction (E) begins to separate from the bottom of tank reflection (D) at large offsets. This causes errors in picking resulting in a higher EM wave velocity, underestimating water content and depth to reflectors, which was observed by Mangel et al. (2011). However, a more accurate characterization of this system was attained through time-lapse monitoring which allowed the system to be imaged at multiple hydrologic states.

GPR data dependencies on hydrologic state are prevalent throughout the thin layer experiment. At early times (Figure 3.9c), the layer reflection is assumed to be coincident with the groundwave and is not visible on the data. A simple analysis of this multi-offset data may lead to the conclusion of a single layer system, however, by applying a flux of water to this system, we were able to observe the layer reflection at late

times (Figures 3.0e-f). Given the opposite conditions, at late times, the bottom of tank reflection (G) is not visible on the data due to interference from the side of tank reflection (J) and layer multiple (2E), leading again to misinterpretation of the radar data due to hydrologic state, however, if the system was imaged at initial conditions (Figure 3.9c), the bottom of tank reflection would be clearly identified.

The elimination of error in GPR data analysis is especially important to the identification of UXOs. Wilson et al. (2007) explored the detection capabilities of significantly different algorithms, involving edge features, Markov models, geometric features, and spectral features. Regardless of the wide spectrum of approaches for data signal processing, a 90% probability of detection was the highest probability attained. While this is exceptionally high, there is still room for improvement, which may be filled by exploring the changes in these responses as a function of hydrologic state, in order to account for them in the data analysis. The land mine surrogate showed promise for these effects as significant differences were seen in the amplitude vs. offset relationships when compared with the homogeneous case, while more subtle differences were observed with changes in hydrology. More research is needed in this field, in order to accurately determine how these responses change with hydrologic state and build the effect into the pattern recognition algorithms.

This time-lapse monitoring of dynamic hydrologic processes such as infiltration also shows promise for quantifying preferential flow through the observation of propagating wetting fronts. Although not observed on the GPR data, there is evidence which may be linked to preferential flow phenomenon in the moisture probe data. For

the layered tank experiment, it is clear from the abnormally high water content probe readings at late experiment times (>100min) for the central probe array (Figure 3.8) that positive head has built up here, and saturation has been attained. This causes pronounced three-dimensional flow outward from the volume under the irrigation grid, spreading water to the perimeter of the tank. Unsaturated flow is typically conceptualized as one-dimensional (Huang et al., 2011, Inoue et al., 2000, Varado et al., 2006), and was adequate for Mangel et al. (2011); however, more robust computational models will be needed to numerically represent this process as water is building at the interface between the layers in a non-uniform fashion, greatly increasing the chances for preferential flow paths to develop. Evidence for preferential flow can be seen in the central probe and 0.2m lateral probe array data (Figure 3.8). The central probe at 0.25m never responds to the infiltrating water, however, the central probes at 0.35m and 0.45m respond late in the experiment (150-160min). This same behavior was seen in a comparatively homogeneous system by Haarder et al., 2011, where the authors monitored an infiltration experiment using a dyed tracer and surface-based GPR profiling. Subsequent to the experiment, the area was excavated and revealed volumes of the subsurface that the dyed tracer flowed around. These phenomena strengthen the argument for a more robust way of characterizing the vadose zone as these heterogeneous distributions of water in a physically homogeneous media play a role in flow and transport of subsurface fluids.

3.8.Conclusions

It has been shown that the response of ground-penetrating radar is highly dependent on the hydrology of the subsurface being sampled for homogeneous systems,

and discrete and continuous heterogeneities in a homogeneous background media. Three experiments were performed involving the transient imaging of 1) a homogeneous system, 2) a landmine surrogate, and 3) a thin layer of silica flour during controlled hydrologic perturbations to qualitatively determine 1) if these heterogeneities are visible on WARR data, 2) how these signatures differ from a homogeneous system, 3) if simple predictive modeling is sufficient to estimate the GPR response, and 4) how signatures of these heterogeneities change for different hydrologic states.

WARR imaging of the homogeneous tank showed changes in the groundwave and bottom of tank reflection associated with changes in the average water content of the tank. However, WARR imaging of the layered tank at early times failed to show separation of the layer reflection and the groundwave, inhibiting simple data interpretation. The same was true for the buried land mine as the land mine reflection and groundwave arrivals were never clearly isolated from each other, however, WARR imaging showed promise for both experiments at late times (high water content and low EM wave velocity) as the layer reflection separated from the groundwave and the land mine signal remained as the ground wave was attenuated. Amplitude vs. offset relationships for the land mine surrogate showed high dependencies between amplitude and offset, but also indicated that hydrologic conditions have an effect on the amplitude of the arrival.

More reliable and versatile data sets could be collected using common mid-point surveying, common offset profiling, or full 3D imaging of these heterogeneities using multi-channel radar systems in order to sample more points in the subsurface as this may

lead to identification of preferential flow paths and provide a more reliable characterization of the vadose zone. Analytical modeling introduced here provided a basic understanding of arrivals on GPR data and offered insight into further data processing procedures. This model did an exceptional job at indicating reflections for the layer and bottom of tank, however, further processing of the data is needed in order to isolate these signals and determine how they respond to changing hydrologic conditions. Regardless of the simplicity of this form of data interpretation, it offers a path forward for the analysis of heterogeneities on GPR data and motivates the use of full 3D imaging and robust signal processing algorithms.

4. Conclusions

Three experiments were conducted to determine the ability of ground-penetrating radar (GPR) to non-invasively determine water content while simultaneously extracting data to resolve depth to wetting fronts and stratigraphic boundaries. It was also shown that the GPR response is highly dependent on the hydrologic state of the subsurface, and time-lapse monitoring of systems at multiple hydrologic states may help to eliminate errors from radar data interpretation. The systems studied included 1) a homogeneous tank of river sand, 2) homogeneous river sand with an embedded layer of silica flour, and 3) homogeneous river sand with an embedded land mine surrogate, were subjected to controlled irrigation events and monitored with GPR using WARR surveying. The unique form of data collection allowed the data to be conceptualized into a 3D data cube, with axes of experiment time (min), travel time (ns) and antenna offset (m). Multi-offset and transient common-offset projections were generated to extract EM wave velocities through NMO analysis and observe changes in arrivals with variably hydrologic conditions, respectively.

For the homogeneous river sand tank, NMO analysis was employed to determine changes in electromagnetic wave velocities due to changes in average water content of the tank. Average water content measurements from in-situ moisture probes were in good agreement with estimates determined using the GPR data. Differences on the order of 3-5% (vol. vol.$^{-1}$) were assumed to be associated with errors in data analysis caused by wave interference. This same effect was seen on the depth to wetting front and depth to bottom of tank estimates, with the maximum of all errors occurring during infiltration of

the irrigated water. It was concluded that the conceptualization of unsaturated flow in 1D was adequate in the sense that it was in fair agreement with experimental values, however, more exhaustive GPR data collection must be employed to fully capture dynamic processes and constrain boundaries. This rich data set will allow for inversion of the GPR data, providing higher quality images and a more robust analysis. This presents a significant opportunity for non-invasively monitoring vadose zone dynamics at catchment scales at time scales coincident with individual hydrologic perturbations, e.g. rainfall.

The approach to analyzing the layer and buried land mine experiments was to take a step away from robust numerical methods, and rely on analytical models to determine the capability of the radar to delineate these common heterogeneities, while qualitatively assessing the hydrologic response from the in-situ capacitance probes. The layered tank had a significantly different hydrologic response due to the low hydraulic conductivity of the silica flour, confirmed by the build-up of positive head above the layer, which caused a highly heterogeneous distribution of water, contributing to multiple occurrences of preferential flow. The buried land mine surrogate tank responded in a nearly identical fashion as the homogeneous tank, with small differences arising from differences in the applied flux rate and initial conditions. In a similar way, the GPR response of the land mine tank mimicked the homogeneous tank, while the GPR response from the layered tank was clearly different. While simple models were able to identify most arrivals in both experiments, this approach, coupled with WARR data collection, falls short of isolating and analyzing the individual arrivals. However, this approach was very useful

in determining the source of arrivals, causes for changes in amplitude, and determining a coarse estimate of electromagnetic wave velocities. Continuing research will focus on alleviating issues outlined in this text, calibrating hydrologic models with GPR data, and identifying buried targets using neural networks.

Main issues hindering the progress of this research are 1) wave interference, 2) signal processing and analysis, and 3) survey geometry. Wave interference caused by the boundaries of the experimental tank can obviously be alleviated by changing the proximity of the antennas to the wall; however, interference caused by the refraction of energy at interfaces and transient reflectors (e.g. wetting fronts) is unavoidable at laboratory and field scales and will need to be accounted for in data analysis. These more robust signal processing and analysis algorithms will be developed in MATLAB and offer an objective analysis of the GPR data. Multiple filters, e.g. AGC gain or bandwidth filtering, applied to GPR data are currently coded in MATLAB, offering a solid foundation for the coupling of signal processing and data analysis functions.

While WARR data collection is aptly capable of sampling and imaging of subsurface heterogeneities, other approaches are available, such as common mid-point (CMP) surveys, which do not assume flat and continuous boundaries. This new approach to this research will involve 1) the construction of a multi-axes positioning system to replace the current uni-axial system, 2) construction of a larger tank to eliminate boundary effects, 3) CMP and common offset data collection in 4D, 4) the development of coupled hydrologic and geophysical models, and 5) development of pattern recognition software for automated detection of buried objects.

Works Cited

Al-Nuaimy, W., Huang, Y., Nakhkash, M., Fang, M.T.C., Nguyen, V.T., Eriksen, A., "Automatic detection of buried utilities and solid objects with GPR using neural networks and pattern recognition", Journal of Applied Geophysics, vol. 43, pp. 157-165, 2000.

Angulo-Jaramillo, R., Vandervaere, J-P., Roulier, S., Thony, J-L., Gaudet, J-P., Vauclin, M., "Field measurement of soil surface hydraulic properties by disc and ring infiltrometers: A review and recent developments," Soil & Tillage Research, vol. 55, pp 1-20, 2000.

Annan, A.P., "Ground-penetrating radar: Principles, procedures, and applications." Sensors and Software Inc. Technical Paper, 2003.

Baker G., "Applying AVO analysis to GPR data," Geophys Res Lett, vol. 25, no. 3, pp. 397-400, 1998.

Berard B.A., Maillol J.-M., "Multi-offset ground penetrating radar data for improved imaging in areas of lateral complexity – Application at a Native American site," J Appl Geophys, no. 62, pp. 167-177, 2007.

Beres, M. Jr., Haeni, F.P., "Application of ground-penetrating radar methods in hydrogeologic studies," Ground Water, vol. 29, no. 3, pp. 375-386, 1991.

Best, J.L., Ashworth, P.J., Bristow, C.S., Roden, J., "Three-dimensional sedimentary architecture of a large, mid-channel sand braid bar, Jamuna River, Bangladesh", Journal of Sedimentary Research, vol. 73, no. 4, pp. 516-530, 2003.

Bohidar, R.N., Hermance, J.F., "The GPR refraction method," Geophysics, vol. 67, no. 5, pp. 1474-1485, 2002.

Boll, J. van Rijn, R.P.G., Weiler, K.W., Ewen, J.A., Daliparthy, J., Herbert, S.J., Steenhuis, T.S., "Using ground-penetrating radar to detect layers in a sandy field soil", Geoderma, no. 70, pp. 117-132, 1996.

Boniger, U. Tronicke, J., "Improving the interpretability of 3D GPR data using target-specific attributes: application to tomb detection", Journal of Archaeological Science, vol. 37, pp. 360-367, 2010.

Bonomo, N., Cedrina, L., Osella, A., Ratto, N., "GPR prospecting in a prehispanic village, NW Argentina", Journal of Applied Geophysics, vol. 67, pp 80-87, 2009.

Booth, A.D., Clark, R. Murray, T., "Semblance response to a ground-penetrating radar wavelet and resulting errors in velocity analysis," Near Surface Geophysics, vol. 8, pp. 235-246, 2010.

Bradford J.H., "Measuring water content heterogeneity using multifold GPR with reflection tomography," Vadose Zone J, vol. 7, no. 1, pp. 184-193, 2008.

Brewster M. L., A.P. Annan A.P., Greenhouse J.P., Kueper B. H,. Olhoeft G.R, Redman J.D., Sander K.A., 'Observed migration of a controlled DNAPL release by geophysical methods," Ground Water, vol. 33, no. 6, pp. 977-987, 1995.

Busch, S., J. van der Kruk, J. Bikowski, H. Vereecken, 2010, Full-waveform inversion of muti-offset surface GPR data, Proceedings of the 13th International Conference on Ground Penetrating Radar, Lecce, Italy, June 21-25, 2010.

Burger, H.R., Sheehan, A.F., Jones, C.H., Introduction to Applied Geophysics: Exploring the Shallow Subsurface. W.W. Norton and Company, New York, NY, USA, 2006.

Cassiani G., Binley A., "Modeling unsaturated flow in a layered formation under quasi-steady state conditions using geophysical data constraints," Adv Water Resour, no. 28, pp. 467-477, 2005.

Chant, I., Lee, D., Ireland,D., "DSTO landmine detection test targets", DSTO Systems Sciences Laboratory, 2005.

Davis, J.L., Annan, A.P., "Ground-penetrating radar for high-resolution mapping of soil and rock stratigraphy," Geophysical Prospecting, vol. 37, is. 5, pp. 531-551, 1989.

Ellsworth,T.R., Jury, W.A, Ernst, F.F., Shouse, P.J., "A three-dimensional field study of solute transport through unsaturated, layered, porous media, 1. Methdology, mass recovery, and mean transport," Water Resources Research, vol. 27, no. 5, pp. 951-965, 1991.

Fisher E., McMechan G.A., Annan P., "Acquisition and processing of wide-aperture ground-penetrating radar data," Geophysics, vol. 57, no. 3, pp. 495-504, 1992.

Flury, M., Fluhler, H., Jury, W.A., Leuenberger, J., "Susceptibility of soils to preferential flow of water: A field study", Water Resources Research, vol. 30, no. 7, pp. 1945-1954, 1994.

Freeland R.S., Yoder, R.E., Ammons, J.T., "Mapping shallow underground features that influence site-specific agricultural production", J Appl Geophys, 40, pp. 19-27, 1998.

Freeland R.S., Odhiambo L.O., Tyner J.S., Ammons J.T., and Wright W.C., "Nonintrusive mapping of near-surface preferential flow", Applied Engineering in Agriculture, 22, pp.315-319, 2006.

Gader P., Lee W.H., Wilson J.N., "Detecting landmines with ground-penetrating radar using feature-based rules, order statistics, and adaptive whitening," IEEE Transactions on Geoscience and Remote Sensing, vol. 42, no. 11, pp. 2522-2534, 2004.

Gerke, H.H., van Genuchten, M.T., "A dual-porosity model for simulating the preferential movement of water and solutes in structured porous media", Water Resources Research, vol. 29, no. 2, pp. 305-319, 1993.

Gish, T.J., Dulaney, W.P., Kung, K.J.S, Daughtry, C.S.T., Doolittle, J.A., Miller, P.T., "Evaluating use of ground-penetrating radar for identifying subsurface flow pathways", Soil Science Society of America Journal, vol. 66, pp. 1620-1629, 2002.

Glass, R.J., Nicholl, M.J., "Physics of gravity fingering of immiscible fluids within a porous media: An overview of current understanding and selected complicating factors," Geoderma, vol. 70, pp. 133-163, 1996.

Gloaguen, E., Chouteau, M., Marcotte, D. Chapuis,R., "Estimation of hydraulic conductivity of an unconfined aquifer using cokriging of GPR and hydrostratigraphic data," Journal of Applied Geophysics, vol. 47, pp 135-152, 2001.

Grasmueck M., Marchesini P., Eberli G.P., Zeller M., VanDam R.L., "4D tracking of water infiltration in fractured high-porosity limestone," in 2010 13th International Conference on Ground Penetrating Radar, Issue Date 21-25 June 2010, pp. 1-6, 2010.

Greaves R.J., Lesmes D.P., Lee J.M., Toksoz M.N., "Velocity variations and water content estimated from multi-offset ground-penetrating radar," Geophysics, vol. 61, no. 3, pp. 683-695, 1996.

Grote K., Hubbard S., Harvey J., Rubin Y., "Evaluation of infiltration in layered pavements using surface GPR reflection techniques," J Appl Geophys, no. 57, pp. 129-153, 2005.

Grote, K., Anger, C., Kelly, B., Hubbard, S., Rubin, Y., "Characterization of soil water content variability and soil texture using GPR groundwave techniques," Journal of Environmental Engineering Geophysics (JEEG), vol. 15, is. 3, pp 93-110, 2010.

Haarder E.B., Looms M.C., Jensen K.H., Nielsen L., "Visualizing unsaturated flow phenomena using high-resolution reflection ground penetrating radar," Vadose Zone J, vol. 10, pp. 84-97, 2011.

Ho, K.C., Collins, L.M., Huettel, L.G., Gader, P.D., "Discrimination mode processing for EMI and GPR sensors for hand-held land mine detection", IEEE Transactions on Geoscience and Remote Sensing, vol. 42, no. 1, pp. 249-263, 2004.

Huang, M., Barbour, L., Elshorbagy, A., Zettl, J.D., Si, B.C., "Infiltration and drainage processes in multi-layered coarse soils", Canadian Journal of Soil Science, vol. 91, pp. 196-183, 2011.

Hubbard, S.S., Rubin, Y., Majer, E., "Ground-penetrating radar-assisted saturation and permeability estimation in bimodal systems," Water Resources Research, vol. 33, no. 5, pp. 971-990, 1997.

Huisman J.A., Sperl C., Bouten W., Verstraten J.M., "Soil water content measurements at different scales: accuracy of time domain reflectometry and ground-penetrating radar," J Hydrol, no. 245, pp. 48-58, 2001.

Huisman J.A., Hubbard S.S., Redman J.D., and Annan A.P., "Measuring soil water content with ground penetrating radar", Vadose Zone J, no. 2, pp. 476-491, 2003.

Inoue, M. Simunek, J., Shiozawa, S., Hopmans, J.W., "Simultaneous estimation of soil hydraulic and solute transport parameters from transient infiltration experiments", Advances in Water Resources, vol. 23, pp. 677-688, 2000.

Irving J., Knight R., "Numerical modeling of ground-penetrating radar in 2-D using MATLAB," Computers and Geosciences, no. 32, pp 1274-1258, 2006.

Jol, H.M. Ground Penetrating Radar: Theory and Applications. Slovenia: Elsevier, 2009.

Jonard, F., Weihermuller, L., Jadoon, K.Z., Schwank, M., Vereecken, H., Lambot, S., "Mapping field-scale soil moisture with L-band radiometer and ground-penetrating radar over bare soil", IEEE Transactions on Geoscience and Remote Sensing, vol. 49, no. 8, pp.2863-2875, 2011.

Knight, R., "Ground-penetrating radar for environmental applications," Annual Review of Earth Planetary Science, vol. 29, pp. 229-255, 2001.

Kung, K.J.S, "Preferential flow in a sandy vadose zone: 1. Field observation", Geoderma, vol. 46, pp. 51-58, 1990.

Lambot S., Binley A., Slob E., Hubbard S., "Ground-penetrating radar in Hydrogeophysics," Vadose Zone J, vol. 7, no. 1, pp. 137-139, 2008.

Lunt I. A., Hubbard S.S., Rubin Y., "Soil moisture content estimation using ground-penetrating radar reflection data," J Hydrol, no. 307, pp. 254-269, 2005.

Looney, B.B, Falta, R.W., Vadose Zone: Science and Technology Solutions. Batelle Press, Columbus, OH, 2000.

Mallants, D., Mohanty, B.P, Jacques, D., Feyen, J., "Spatial variability of hydraulic properties in a multi-layered soil profile," Soil Science, vol. 161, is. 3, pp.167-181, 1996.

Mangel, A.R., Moysey, S.M.J, Ryan, J.C., Tarbutton, J.A., "Multi-offset ground-penetrating radar imaging of a lab-scale infiltration test", Hydrology and Earth Systems Science Discussions, vol. 8, pp. 10095-10123, 2011.

Minet, J., S. Lambot, E.C. Slob, M. Vanclooster, Soil surface water content estimation by full-waveform inversion in the presence of thin layers, IEEE Transactions On Geoscience and Remote Sensing, vol. 48, no. 3, pp. 1138-1150, 2010.

Maxwell, J.C., "On the physical lines of force: Parts I-IV," The London, Edinburgh, and Dublin Philosophical Magazine and Journal of Science, 1861, 1862.

McLay, C.D.A., Dragten, R., Sparling, G., Selvarajah, N., "Predicting groundwater nitrate concentrations in a region of mixed agricultural land use: a comparison of three approaches," Environmental Pollution, vol. 115, pp. 191-204, 2001.

Mohanty, B.P., Ankeny, M.D., Horton, R., Kanwar, R.S., "Spatial analysis of hydraulic conductivity measured using disc infiltrometers", Water Resources Research, vol. 30, no. 9, pp. 2489-2498, 1994.

Moysey S., "Hydrologic trajectories in transient ground-penetrating radar reflection data", Geophysics, vol. 75, no. 4, pp. 211-219, 2010.

Neal,A., "Ground-penetrating radar and its use in sedimentology: principles, problems, and progress," Earth-Science Reviews, vol. 66, is. 3-4, pp. 261-330, 2004.

Neidel, N.S., Taner, M.T., "Semblance and other coherency measures for multichannel data," Geophysics, vol. 36, no. 3, pp. 482-497, 1971.

Oostrom, M. Hofstee, C., Lenhard, R.J., Wietsma, T.W., "Flow behavior and residual saturation formation of liquid carbon tetrachloride in unsaturated heterogeneous porous media," Journal of Contaminant Hydrology, vol. 64, pp. 93-112, 2003.

Pantazidou, M., Sitar, N., “Emplacement of nonaqueous liquids in the vadose zone,” Water Resources Research, vol. 29, no. 3, pp. 705-722, 1993.

Pettinelli, E., Di Matteo, A., Mattei, E., Crocco, L., Soldovieri, F., Redman, J.D., Annan, A.P., “GPR response from buried pipes: measurement on field site and tomographic reconstructions”, IEEE Transactions on Geoscience and Remote Sensing, vol. 47, no. 8, pp. 2639-2645, 2009.

Porsani, J.L., Slob, E., Lima, R.S., Leite, N.D., “Comparing detection and location performance of perpendicular and parallel broadside GPR antenna orientations”, Journal of Applied Geophysics, vol. 70, pp. 1-8, 2010.

Richards, L.A, “Capillary conduction of liquids through porous mediums,”Physics, vol. 1 pp. 318-333, 1931.

Ritsema, C.J., Dekker, L.W., Hendrickx, J.M.H., Hamminga, W., “Preferential flow mechanism in a water repellent sandy soil”, Water Resources Research, vol. 29, no. 7, pp. 2183-2193, 1993.

Rodrigues, S.I., Porsani, J.L., Santos, V.R.N., DeBlasis, P.A.D., Giannini, P.C.F., “GPR and inductive electromagnetic surveys applied in three coastal *sambaqui* (shell mounds) archaeological sites in Santa Catarina state, South Brazil”, Journal of Archaeological Science, vol. 36, pp. 2081-2088, 2009.

Saintenoy A., Schneider S., Tucholka P., “Evaluating ground-penetrating radar use for water infiltration monitoring,” Vadose Zone J, vol. 7, no. 1, pp. 208-214, 2008.

Scanlon, B.R., “Moisture and solute flux along preferred pathways characterized by fissured sediments in desert soils,” Journal of Contaminant Hydrology, vol. 10, is. 1, pp 19-46, 1992.

Schapp, M.G., Leij, F.J., “Improved prediction of unsaturated hydraulic conductivity with the Mualem-van Genuchten model”, Soil Science Socienty of America Journal, vol. 64, pp 843-854, 2000.

Secunda, S., Collin, M.L., Melloul, A.J., “Groundwater vulnerability assessment using a composite model combining DRASTIC with extensive agricultural land use in Israel’s Sharon region,” Journal of Environmental Management, vol. 54, pp. 39-57, 1998.

Simunek, J., van Genuchten, M.T., “Estimating unsaturated soil hydraulic properties from tension disc infiltrometer data by numerical inversion,” Water Resources Research, vol. 32, no. 9, pp. 2683-2696, 1996.

Simunek J., van Genuchten M. Th., Sejna M., HYDRUS 1D Code for simulating the one-dimensional movement of water, heat, and multiple solutes in variably saturated porous media, Department of Environmental Sciences and University of California Riverside, US Salinity Laboratory, USDA, ARS, Riverside, CA, 2005.

Smith, D.G., Jol, H.M., "Ground-penetrating radar investigation of a Lake Bonneville delta, Provo level, Brigham City, Utah", Geology, vol. 20, pp. 1083-1086, 1992.

Steelman, C.M., Endres, A.L., "An examination of direct ground wave soil moisture monitoring over an annual cycle of soil conditions," Water Resources Research, vol. 46, W11533, 2010

Stolte, J., Freijer, J.I., Bouten, W., Dirksen, C., Halbertsma, M., Van Dam, J.C., Van den Berg, J.A., Veerman, G.J., Wosten, J.H.M., "Comparison of six methods to determine unsaturated soil hydraulic conductivity", Soil Science Society of America Journal, vol. 58, pp. 1596-1603, 1994.

Topp G.C., Davis J.L., Annan A.P., "Electromagnetic determination of soil water content: measurements in coaxial transmission lines," Water Resour Res, vol. 16, no. 3, pp. 574-582, 1980.

Truss S., Grasmueck M., Vega S., and Viggiano D.A., "Imaging rainfall drainage within the Miami oolitic limestone using high-resolution time-lapse ground-penetrating radar", Water Resour Res, 43, doi:10.1029/2005WR004395, 2007.

Varado, N., Braud, I., Ross, P.J., "Development and assessment of an efficient vadose zone module solving 1D Richards equation and including root extraction by plants", Journal of Hydrology, vol. 323, pp. 258-275, 2006.

Van Dam, R.L., Schlager, W., "Identifying causes of ground-penetrating radar reflections using time-domain reflectometry and sedimentological analyses," Sedimentology, vol. 47, pp. 435-449, 2000.

van der Kruk J., "Properties of surface waveguides derived from inversion of fundamental and higher mode dispersive GPR data," IEEE Transactions on Geoscience and Remote Sensing, vol. 44, no. 10, pp. 2908-2915, 2006.

van der Kruk, J., Streich R., Green A.G., "Properties of surface waveguides derived from separate and joint inversion of dispersive TE and TM GPR data", Geophysics, vol. 71, iss. 1, pp K19-K29, 2006.

van der Kruk, J., Vereecken, H., Jacob, R.W., "Identifying dispersive GPR signals and inverting for surface wave-guide properties", The Leading Edge, vol. 28, pp.936-940, 2009.

van der Kruk, J., Steelman C.M., Endres, A.L., Vereecken, H., "Dispersion inversion of electromagnetic pulse propagation within freezing and thawing soil waveguides", Geophysical Research Letters, vol. 36, article no. L18503, DOI: 10.1029/2009GL039581, 2009.

van der Kruk, J., Jacob, R.W., Vereecken, H., "Properties of precipitation-induced multilayer surface waveguides derived from inversion of dispersive TE and TM GPR data", Geophysics, vol. 75, iss. 4, pp. WA263-WA273, DOI: 10.1190/1.3467444, 2010.

van Genuchten, M. Th., "A closed-form equation for predicting the hydraulic conductivity of unsaturated soils," Soil Science Society of America Journal, vol. 44, no. 5, pp. 892-898, 1980.

van Overmeeran, R.A., "Radar facies of unconsolidated sediments in The Netherlands: A radar stratigraphy interpretation method for hydrogeology," Journal of Applied Geophysics, vol. 40, pp 1-18, 1998.

van Overmeeren R.A., Sariowan, S.V., Gehrels, J.C., "Ground penetrating radar for determining volumetric soil water content; Results of comparative measurements at two test sites," J Hydrol, vol: 197, issue: 1-4, pp. 316-338, 1997.

Vellidis, G., Smith, M.C., Thomas, D.L., Asmussen, L.E., "Detecting wetting front movement in a sandy soil with ground-penetrating radar", Transactions of the American Society of Agricultural Engineers, vol. 33, iss. 6, pp. 1867-1874, 1990.

Vervoort, R.W., Radcliffe, D.E., West, L.T., "Soil structure development and preferential solute flow", Water Resources Research, vol. 35, no. 4 pp. 913-928, 1999.

Wierenga, P.J., Hills, R.G., Hudson, D.B., "The Las Cruces Trench Site: Characterization, experimental results, and one-dimensional flow predictions," Water Resources Research, vol.27, no.10, pp. 2695-2705, 1991.

Wilson, J.N., Gader, P. Lee, W.H., Frigui, H., Ho, K.C., "A large-scale systematic evaluation of algorithms using ground-penetrating radar for landmine detection and discrimination", IEEE Transactions on Geoscience and Remote Sensing, vol. 45, no. 8, pp. 2560-2572, 2007.

Yilmaz O., Seismic Data Analysis: Processing, Inversion, and Interpretation of Seismic Data, SEG Investigations in Geophysics 2, Society of Exploration Geophysicists, Tulsa, OK. , 1987

Zeng, X., McMechan, G.A., “GPR characterization of buried tanks and pipes”, Geophysics, vol. 62, no. 3, pp. 797-806, 1997.